

1 **Autophagy adaptors mediate Parkin-dependent mitophagy by forming**
2 **sheet-like liquid condensates**

3

4 Zi Yang^{1,a}, Saori R. Yoshii¹, Yuji Sakai^{1,2,3,b}, Jing Zhang¹, Haruka Chino^{1,c}, Roland L.
5 Knorr^{1,4,d}, Noboru Mizushima^{1,5*}

6

7 ¹Department of Biochemistry and Molecular Biology, Graduate School of Medicine, The
8 University of Tokyo, Tokyo, Japan.

9 ²Department of Biosystems Science, Institute for Life and Medical Sciences, Kyoto
10 University, Sakyo-ku, Kyoto, Japan

11 ³Interdisciplinary Theoretical and Mathematical Sciences (iTHEMS) Program, RIKEN,
12 Wako, Saitama, Japan

13 ⁴Institute of Biology, Humboldt-Universität zu Berlin, Berlin, Germany

14 ⁵International Research Center for Neurointelligence (WPI-IRCN), UTIAS, The University of
15 Tokyo, Tokyo, Japan

16 ^aPresent address: Leibniz Forschungsinstitut für Molekulare Pharmakologie (FMP) , Berlin,
17 Germany

18 ^bPresent address: School of Science/Graduate School of Nanobioscience, Yokohama City
19 University, Yokohama, Japan

20 ^cPresent address: Department of Cell Biology, Harvard Medical school, Boston, MA, USA

21 ^dPresent address: University of Cologne, Faculty of Medicine and University Hospital
22 Cologne

23

24 *Corresponding author. Department of Biochemistry and Molecular Biology, Graduate
25 School of Medicine, The University of Tokyo, 7-3-1 Hongo, Bunkyo-ku, Tokyo 113-0033,
26 Japan; Tel: +81-3-5841-3440; Fax: +81-3-3815-1490; E-mail: nmizu@m.u-tokyo.ac.jp

27 **Abstract**

28 During PINK1- and Parkin-mediated mitophagy, autophagy adaptors are recruited to
29 damaged mitochondria to promote their selective degradation. Autophagy adaptors such as
30 optineurin (OPTN) and NDP52 facilitate mitophagy by recruiting the autophagy-initiation
31 machinery, and assisting engulfment of damaged mitochondria through binding to
32 ubiquitinated mitochondrial proteins and autophagosomal ATG8 family proteins. Here, we
33 demonstrate that OPTN and NDP52 form sheet-like phase-separated condensates with
34 liquid-like properties on the surface of ubiquitinated mitochondria. The dynamic and liquid-
35 like nature of OPTN condensates is important for mitophagy activity, because reducing the
36 fluidity of OPTN-ubiquitin condensates suppresses the recruitment of ATG9 vesicles and
37 impairs mitophagy. Based on these results, we propose a dynamic liquid-like, rather than a
38 stoichiometric, model of autophagy adaptors to explain the interactions between autophagic
39 membranes (i.e., ATG9 vesicles and isolation membranes) and mitochondrial membranes
40 during Parkin-mediated mitophagy. This model underscores the importance of liquid-liquid
41 phase separation in facilitating membrane-membrane contacts, likely through the
42 generation of capillary forces.

43

44 **Keywords**

45 autophagy; mitophagy; liquid–liquid phase separation; optineurin; wetting

46

47 **Introduction**

48 Macroautophagy (hereafter referred to as autophagy) is an intracellular degradation
49 process mediated by a double-membraned organelle termed the autophagosome
50 (Nakatogawa, 2020; Mizushima & Levine, 2020). Cytosolic components such as proteins
51 and organelles are segregated into autophagosomes, which subsequently fuse with
52 lysosomes for degradation. Autophagy can be either non-selective or selective (Lamark &
53 Johansen, 2021; Vargas *et al*, 2023). Mitophagy, which is a selective type of autophagy,
54 specifically degrades mitochondria and can be induced by mitochondrial damage or cellular
55 stresses (Onishi *et al*, 2021; Ganley & Simonsen, 2022). For example, upon mitochondrial
56 damage, numerous mitochondrial outer-membrane proteins are ubiquitinated by the
57 PINK1-Parkin system, initiating the recruitment of autophagy adaptors, including optineurin
58 (OPTN), calcium binding and coiled-coil domain 2 (CALCOCO2/NDP52), sequestosome 1
59 (SQSTM1/p62), Next to BRCA1 gene 1 protein (NBR1), and Tax1 binding protein 1
60 (TAX1BP1) (Lamark & Johansen, 2021; Vargas *et al*, 2023). These autophagy adaptors
61 bridge the mitochondrial and autophagosomal membranes by interacting with mitochondrial
62 ubiquitinated proteins via a ubiquitin-binding domain (UBD) and with autophagosomal
63 ATG8 family proteins (i.e., LC3 and GABARAP family proteins in mammals) via the LC3-
64 interacting region (LIR). In addition to their role in supporting efficient engulfment by
65 autophagosomes, OPTN and NDP52 also play crucial roles in inducing mitophagy by
66 recruiting upstream autophagy factors (Lazarou *et al*, 2015); OPTN recruits ATG9 vesicles
67 and TBK1, which subsequently recruits the PI3K complex, whereas NDP52 recruits the
68 ULK1 complex through interaction with FIP200 (Yamano *et al*, 2020, 2024; Nguyen *et al*,
69 2023; Vargas *et al*, 2023).

70 Liquid–liquid phase separation (LLPS) has been described in various biological
71 processes (Musacchio, 2022; Hirose *et al*, 2023). LLPS involves the formation of liquid-like
72 condensates through dynamic, multivalent interactions between various molecules that
73 often possess intrinsically disordered regions. Emerging evidence suggests connections
74 between autophagy and LLPS at multiple steps, including autophagosome formation and

75 degradation (Noda *et al*, 2020; Ma *et al*, 2023). Notably, autophagy adaptors, such as p62,
76 undergo LLPS through multivalent interaction with poly-ubiquitins and form cytosolic
77 condensates (Zaffagnini *et al*, 2018; Sun *et al*, 2018). These condensates can be degraded
78 by autophagy, which is termed “fluidophagy” (Agudo-Canalejo *et al*, 2021). Furthermore,
79 recent studies showed that p62 undergoes LLPS on mitochondria and lysosomes that are
80 subjected to selective autophagy (Peng *et al*, 2021; Gallagher & Holzbaur, 2023).

81 Generally, phase-separated condensates can deform when they contact a rigid surface
82 in order to minimize the overall energy of the system, a phenomenon known as “wetting”
83 (Kusumaatmaja *et al*, 2021b; Gouveia *et al*, 2022). The wetting behavior of intracellular
84 condensates is determined by the interfacial tensions between the condensate–membrane,
85 condensate–cytosol, and cytosol–membrane interfaces. Depending on the relative
86 strengths of these interfacial tensions, the condensates exhibit partial wetting, complete
87 wetting, or de-wetting. In contrast, elastic surfaces, including membranes to which phase-
88 separated condensates adhere, also deform (Kusumaatmaja *et al*, 2021a, 2021b; Gouveia
89 *et al*, 2022; Mangiarotti *et al*, 2023). This indeed happens during fluidophagy;
90 autophagosomal membranes bend along the surface of p62 condensates (Agudo-Canalejo
91 *et al*, 2021). Deformation of a membrane by a phase-separated condensate is determined
92 by the energy balance between membrane deformation and the surface tension of the
93 condensate, which is known as elastocapillarity (Style *et al*, 2017; Kusumaatmaja *et al*,
94 2021b; Mangiarotti *et al*, 2023).

95 By forming capillary bridges, wetting droplets can also induce adhesion of surfaces
96 (Wexler *et al*, 2014). Whether LLPS and capillary bridges also contribute to the adhesion of
97 cellular membranes is not presently known. Therefore, we hypothesized that phase-
98 separated condensates of autophagy adaptors can wet both mitochondria and autophagic
99 membranes, including ATG9 vesicles and isolation membranes (also called phagophores),
100 thereby promoting their contact during Parkin-mediated mitophagy. In this study, we employ
101 live-cell imaging and a mathematical model to provide evidence that the autophagy
102 adaptors form phase-separated condensates on the surface of the mitochondrial

103 membrane, resulting in sheet-like condensates that cover the surface of ubiquitinated
104 mitochondria upon mitophagy induction. These condensates accumulate between
105 mitochondria or between mitochondria and autophagic membranes, exhibiting a dynamic
106 nature with a liquid-like property. Furthermore, we demonstrate the essential role of these
107 dynamic condensates in the recruitment of ATG9 vesicles and the initiation of mitophagy.
108 Based on these results, we propose a dynamic liquid-like model, rather than a
109 stoichiometric model, to describe the roles of autophagy adaptors in Parkin-mediated
110 mitophagy.

111

112 **Results**

113

114 **Autophagy adaptors show distinct distributions during Parkin-mediated mitophagy**

115 To better understand the role of each autophagy adaptor, we analyzed their localization
116 during Parkin-mediated mitophagy. When mitophagy was induced by treatment with the
117 mitochondrial uncoupler carbonyl cyanide *m*-chlorophenylhydrazone (CCCP) in HeLa cells
118 expressing exogenous Parkin, the autophagy adaptors p62, OPTN, NBR1, NDP52, and
119 TAX1BP1 translocated to mitochondria as previously observed (Fig. 1A and B) (Geisler *et*
120 *al*, 2010; Wong & Holzbaur, 2014; Heo *et al*, 2015; Moore & Holzbaur, 2016; Gallagher &
121 Holzbaur, 2023). Ubiquitin and all of these autophagy adaptors were distributed evenly on
122 the surface of separate mitochondria (Mt; Fig. 1A). In contrast, these adaptors exhibited
123 distinct localization patterns during the formation of isolation membranes on mitochondria
124 (Mt–IM; Fig. 1B and C). The signals of OPTN and NDP52 were enriched in areas where
125 LC3B signals colocalized, while they were mostly absent from the LC3B-negative side of
126 the same mitochondria (Fig. 1B and C). Endogenous OPTN and NDP52 also showed clear
127 enrichment on the LC3B-positive areas in comparison to the LC3B-negative side,
128 confirming that this localization is not caused by the overexpression of adaptors (Fig. 1D).
129 However, this inhomogeneous distribution pattern was not observed for ubiquitin, p62,
130 NBR1, and TAX1BP1 (Fig. 1B and C). Unlike OPTN and NDP52, p62 showed enrichment
131 between clustered mitochondria (Mt–Mt), which is consistent with previous reports (Fig.
132 EV1A and B) (Wong & Holzbaur, 2014), which appears to be consistent with the role of p62
133 in promoting mitochondrial clustering (Narendra *et al*, 2010; Okatsu *et al*, 2010). These
134 accumulation patterns cannot be explained by the stoichiometric interaction of the
135 autophagy adaptors with ubiquitinated proteins that are evenly distributed on mitochondria.

136 The localization of autophagy adaptors may be affected by their interaction with other
137 adaptors (Turco *et al*, 2021; Gubas & Dikic, 2022). To examine the localization of each
138 adaptor on its own, we used HeLa cells lacking all five autophagy adaptors (penta KO cells)
139 to exclude the effect of other adaptors (Lazarou *et al*, 2015). In penta KO cells, OPTN and

140 NDP52 exhibited significant enrichment in LC3B-positive areas, similar to that observed in
141 wild-type cells, suggesting that this accumulation occurred independently of heterologous
142 interaction with other adaptors (Fig. 1E and F). Mitophagy was not restored by exogenous
143 expression of p62 or NBR1 in penta KO cells, and thus colocalization with LC3 could not be
144 tested for these two adaptors (Lazarou *et al*, 2015). The accumulation of p62 between
145 clustered mitochondria was also observed in penta KO cells (Fig. EV1C and D). Given the
146 uniform distribution of ubiquitinated proteins on mitochondrial surfaces, these data suggest
147 that autophagy adaptors exhibit non-stoichiometric enrichment between membranes.
148 Hereafter, we used penta KO cells to study each autophagy adapter individually.

149

150 **OPTN and NDP52 show a dynamic exchange between the mitochondrial surface and**
151 **cytosol**

152 We hypothesized that the non-stoichiometric distribution of the autophagy adaptors on
153 ubiquitinated mitochondria could be explained by LLPS. Typical condensates generated by
154 LLPS exhibit rapid exchange of their components, which is often demonstrated by
155 fluorescence recovery after photobleaching (FRAP) analysis (Taylor *et al*, 2019;
156 McSwiggen *et al*, 2019). We first conducted FRAP experiments for separate (i.e.,
157 unclustered) mitochondria in CCCP-treated cells. As expected, ubiquitin showed virtually no
158 recovery because it was conjugated to mitochondrial membrane proteins (Fig. 2A and B).
159 Additionally, p62 recovered only slightly, suggesting a minute exchange between the
160 mitochondrial surface and cytosol (Fig. 2A and B). In contrast, OPTN and NDP52 showed a
161 rapid recovery, indicating a dynamic exchange of these adaptors between the mitochondrial
162 surface and the cytosol (Fig. 2A and B).

163 Next, we examined the dynamics of adaptors between mitochondria and isolation
164 membranes. OPTN and NDP52 showed partial recovery (Fig. 2C and D). Although this
165 result indicates some exchange of these adaptors between membranes, the incomplete
166 recovery suggests the existence of a gel-like or immobile fraction. Treatment with 1,6-
167 hexanediol, which can be used to dissolve condensates, dispersed OPTN and NDP52, but

168 not p62, from mitochondria without isolation membranes (Fig. 2E, EV2A). In contrast, 2,5-
169 hexanediol, which is considered by some studies as a negative control for 1,6-hexanediol,
170 did not disperse the OPTN or NDP52 condensates (Fig. EV2B). These data suggest that
171 OPTN and NDP52 accumulation is supported by weak interactions. In contrast, OPTN and
172 NDP52 at the mitochondria-isolation membrane contact sites remained unaffected by 1,6-
173 hexanediol (Fig. EV2C). This may be due to the additional interaction with ATG8 proteins,
174 not only with ubiquitin. These results indicate that OPTN and NDP52 on ubiquitinated
175 mitochondria are mobile and can quickly exchange between the mitochondrial surface and
176 the cytosol, supporting the hypothesis that they form phase-separated condensates on
177 damaged mitochondria.

178

179 **Mathematical models of condensate formation and localization of autophagy
180 adaptors**

181 To simulate the behavior of autophagy adaptors in the context of phase-separated
182 condensates, we developed mathematical models (see Materials and Methods for details).
183 First, we considered the case of two mitochondria approaching each other (Fig. 3A). In
184 Parkin-mediated mitophagy, various proteins in the mitochondrial outer membrane are
185 ubiquitinated. We modeled the mitochondrial outer membrane as a circle with a diameter of
186 $D_{Mt} = 600$ nm. On these mitochondria, we assumed a ring-shaped ubiquitin layer with a
187 thickness $w_{Ub} = 20$ nm and area-fraction (hereafter referred to as concentration) $\phi_{Ub} = 0.1$
188 (Milo & Phillips, 2015; Berry *et al*, 2018) (Fig. 3A). The closest distance between the two
189 mitochondrial outer membranes was set to d_{Mt} (Fig. 3A). Here, we considered the
190 dynamics of concentration changes of the adapter proteins and solvent components. We
191 assumed that mitochondria were very large compared with proteins and did not move on a
192 similarly short time scale, and that ubiquitin was tightly bound to mitochondrial membranes
193 and immobile, as suggested by the FRAP experiment (Fig. 2B). The adaptor proteins were
194 assumed to diffuse freely in solution and to bind to ubiquitin and themselves (self-
195 interactions) with strengths χ_{Ub} and χ_{self} , respectively. The adaptors showed accumulation

196 and distribution on mitochondria similarly to what was observed in cells (Figure EV1) when
197 $\chi_{Ub} \geq 12k_B T$ and $\chi_{self} = 3k_B T$ (Figure. EV3A), with the Boltzmann constant k_B and
198 temperature T . Therefore, we used $\chi_{Ub} = 12k_B T$ and $\chi_{self} = 3k_B T$ for further analyses.

199 Using the mathematical model, we assessed how the condensates deformed when the
200 distance between two mitochondria d_{Mt} was changed. When two mitochondria were far
201 apart ($d_{Mt} = 900$ nm), the model predicted that adaptors cover the entire mitochondrial
202 surface (Fig. 3B). When the mitochondria were close enough to come into contact ($d_{Mt} =$
203 60 nm), the adaptors moved to the area between the mitochondria and filled the cleft
204 between them (arrowheads, Fig. 3B).

205 Next, we considered the case in which a growing isolation membrane surrounded and
206 enclosed a single mitochondrion (Fig. 3C and D). A mitochondrion with ubiquitin was
207 modeled as mentioned above, and the isolation membrane was modeled as a region of
208 thickness $w_{IM} = 50$ nm bound by two semicircles with the same center as the
209 mitochondrion. The closest distance between the isolation membrane and the
210 mitochondrial outer membrane was $d_{IM} = 100$ nm, and the isolation membrane bent at an
211 angle α to surround the mitochondrion. The surface of the isolation membrane was
212 assumed to be covered by an LC3 region with a thickness $w_{LC3} = 20$ nm and concentration
213 $\phi_{LC3} = 0.1$. The adaptors interacted with both LC3 and ubiquitin with strengths χ_{LC3} and
214 χ_{Ub} , respectively. A clear accumulation of the autophagy adaptor in the region in contact
215 with the isolation membrane, along with depletion from the non-contacting region, was
216 observed at $\chi_{LC3} \geq 12k_B T$ (Figure EV3B), similar to the OPTN distribution observed in cells
217 (Fig. 1B). Therefore, we used $\chi_{LC3} = 12k_B T$ for further analyses.

218 Using this model, we determined the distribution of the adaptors when the isolation
219 membrane appeared and elongated (changing the angle α surrounding the mitochondrion).
220 In the absence of the isolation membrane, the adaptors wet the entire mitochondrial
221 surface uniformly (Fig. 3D). However, with the appearance of the isolation membrane, the
222 adaptors remobilized to the area between the isolation membrane and mitochondrion, and
223 this adaptor-enriched region elongated together with the isolation membrane. These

224 modeling results suggest that the distribution of the adaptors on a mitochondrion can
225 change upon contact with another mitochondrion or an isolation membrane.

226

227 **OPTN condensates redistribute upon membrane contact**

228 Our mathematical models predict that the OPTN distribution changes when mitochondria
229 cluster or are engulfed by isolation membranes. We then validated these predictions by
230 using live-cell imaging. When two small mitochondria with uniform OPTN distributions on
231 their surface approached each other, OPTN redistributed and formed a smooth surface that
232 covered the two adjacent mitochondria (Fig. 4A–D, Movie EV1). Notably, strong OPTN
233 enrichment was observed in the cleft between the two mitochondria (arrowheads, Fig. 4A
234 and C), showing a pattern distinct from that of the outer membrane protein Omp25 (OPTN
235 signal peaks localized outside of Omp25 signal peaks) (Fig. 4B and D). This phenomenon
236 was apparent when the size of both (Fig. 4A) or one (Fig. 4C, Movie EV1) of the two
237 mitochondria was less than 1 μm . Although OPTN formed sheet-like rather than spherical
238 condensates, this phenomenon appeared to be similar to condensate coalescence, which
239 is one of the hallmarks of liquid-like condensates (Hyman *et al*, 2014).

240 Furthermore, when an isolation membrane started to engulf a mitochondrion, OPTN,
241 which was initially distributed uniformly on the mitochondrial surface, underwent
242 redistribution to the area contacting the isolation membrane (Fig. 4E, Movie EV2). OPTN
243 signals on the isolation membrane-negative side of the mitochondrion diminished during
244 this process (Fig. 4E and F). The OPTN-enriched region expanded together with the
245 isolation membrane thereafter (Fig. 4E). These live-cell observations are consistent with
246 the predictions of our mathematical models (Fig. 3). Taken together, our experimental data
247 support the hypothesis that OPTN forms sheet-like phase-separated condensates on the
248 surface of ubiquitinated mitochondria, exhibiting liquid-like properties.

249

250 **Liquid-like property of OPTN condensates is required for mitophagy**

251 To investigate the importance of the liquid-like nature of OPTN condensates on

mitochondria, we sought to reduce their fluidity by strengthening the interaction between ubiquitin and GFP–OPTN constructs. To achieve this, we utilized the anti-green fluorescent protein (GFP) nanobody, which exhibits a high binding affinity to GFP (Rothbauer *et al*, 2008) (Fig. 5A). Consequently, the interaction between anti-GFP nanobody-fused ubiquitin and GFP–OPTN was stronger than that between ubiquitin and GFP–OPTN (Fig. 5B). Expression of anti-GFP nanobody-fused ubiquitin (nanobody–mRuby–Ub) did not affect the recruitment of GFP–OPTN to mitochondria (Fig. 5A, (i) and (ii)) but partially reduced its FRAP recovery (Fig. 5C), suggesting a reduction in mobility. We then evaluated the effect of reduced OPTN fluidity on mitophagy using the recently developed HaloTag cleavage assay (Yim *et al*, 2022). This assay utilizes the ligand-dependent conformational change of HaloTag (Halo); ligand-free Halo is efficiently degraded in lysosomes, whereas ligand-bound Halo becomes resistant to lysosomal degradation. When Halo is expressed in the mitochondrial matrix by fusing to the mitochondrial presequence of Fo-ATPase subunit 9 and SNAP-tag (mtHalo–SNAP), we can measure the extent of mitochondrial degradation by quantifying the amount of processed free Halo out of the total amount of Halo (mtHalo–SNAP + processed Halo). Mitophagy activity, which was impaired in penta KO cells, was restored by the expression of GFP–OPTN (Fig. 5D and E). Mitophagy activity was partially reduced in cells expressing GFP-OPTN and nanobody–mRuby–Ub (Fig. 5D and E).

The partial reduction in both FRAP recovery and mitophagy activity may be attributed to the remaining interaction between OPTN and endogenous ubiquitin. Therefore, we deleted the ubiquitin-binding domain in ABINs and NEMO (UBAN domain) from OPTN (GFP–OPTN Δ UBAN), abolishing its interaction with ubiquitinated proteins (Fig. 5B). GFP–OPTN Δ UBAN failed to accumulate on mitochondria in the presence of mRuby–Ub (Fig. 5A, (iii)). In contrast, the expression of nanobody–mRuby–Ub rescued the recruitment of GFP–OPTN Δ UBAN to mitochondria (Fig. 5A, (iv)), albeit to a reduced extent, likely reflecting the loss of condensate formation. FRAP experiments revealed that, compared with wild-type GFP–OPTN (Fig. 5A, (i)), GFP–OPTN Δ UBAN (Fig. 5A, (iv)) showed a substantial decrease in recovery on mitochondria when co-expressed with nanobody–mRuby–Ub, indicating a

280 reduction in its dynamic properties (Fig. 5C). GFP–OPTN Δ UBAN failed to restore
281 mitophagy, even when it was co-expressed with nanobody–mRuby–Ub to rescue ubiquitin
282 binding and mitochondrial localization (Fig. 5A, B, D, and E). This impairment was indeed
283 due to the loss of binding to ubiquitin because a point mutation that abolished ubiquitin
284 binding (E478G) (Li *et al*, 2018) also showed normal mitochondrial localization, low FRAP
285 recovery, and mitophagy defect (Fig. 5D, E, EV4A, and B). Furthermore, the impaired
286 mitophagy was not simply due to the altered binding orientation of OPTN. Replacement of
287 its UBAN domain with GFP (OPTN Δ UBAN–GFP), mimicking its binding to ubiquitin at the
288 C-terminus, did not restore FRAP recovery or mitophagy activity, although it also showed
289 clear recruitment to mitochondria in the presence of nanobody–mRuby–Ub (Fig. EV4A, B,
290 C and D). The restricted orientation of OPTN due to the stoichiometric interaction between
291 GFP and nanobody, as opposed to the more flexible orientation in liquid-like condensates,
292 may also contribute to the impairment of autophagy.

293 Consistent with the results of mitophagy activity, the accumulation of the ULK1
294 complex component FIP200, likely representing isolation membranes, was observed in the
295 presence of mRuby–Ub and GFP–OPTN (Fig. EV5A). In contrast, no clear FIP200
296 accumulation was observed in cells expressing nanobody–mRuby–Ub and GFP–
297 OPTN Δ UBAN, suggesting that mitophagy failed at the initiation step in these cells (Fig.
298 EV5A). Together, these data suggest that the localization of OPTN on mitochondria and its
299 binding to ubiquitin alone is insufficient for mitophagy, and the fluidity of OPTN is important
300 for effective mitophagy induction.

301

302 **Liquid-like property of OPTN condensates is required for initiation of mitophagy by
303 recruiting ATG9 vesicles and activating TBK1**

304 ATG9 vesicles are considered to be one of the sources of autophagosomal
305 membranes (Yamamoto *et al*, 2012). Upon mitophagy induction, ATG9 vesicles accumulate
306 at the sites of autophagosome formation (Itakura *et al*, 2012). OPTN plays a crucial role in
307 this process by recruiting ATG9 vesicles to induce mitophagy (Yamano *et al*, 2020). In

308 general, liquid-like condensates can be involved in clustering small vesicles such as
309 synaptic vesicles, which exemplify complete wetting (Milovanovic & De Camilli, 2017;
310 Sansevrino *et al*, 2023). Indeed, ATG9 vesicles are incorporated into condensates
311 containing a glaucoma-associated OPTN mutant (O'Loughlin *et al*, 2020) and synapsin
312 (Park *et al*, 2023). We, therefore, hypothesized that the liquid-like properties of OPTN
313 condensates on mitochondria facilitate the recruitment of ATG9 vesicles. Consistent with
314 previous reports (Itakura *et al*, 2012; Yamano *et al*, 2020), ATG9A was recruited to
315 depolarized mitochondria in cells expressing GFP–OPTN (Fig. 6A and B). However, this
316 ATG9A recruitment was almost completely abolished in cells expressing nanobody–
317 mRuby–Ub and GFP–OPTNΔUBAN (Fig. 6A and B), even though GFP–OPTNΔUBAN still
318 retains the ATG9A-interacting domain and the ability to bind with the ATG9 vesicles (Fig. 6C
319 and D). These data suggest that the fluidity of sheet-like OPTN condensates on the
320 mitochondrial surface is crucial for recruiting ATG9 vesicles and executing mitophagy.

321 Furthermore, TBK1 is recruited by OPTN to the mitophagy initiation site to be
322 phosphorylated and activated, driving the feed-forward mechanism of OPTN accumulation
323 and TBK1 activation, which in turn phosphorylates the PI3K complex to initiate mitophagy
324 (Nguyen *et al*, 2023; Yamano *et al*, 2024). Consistently, a clear accumulation of
325 phosphorylated TBK1 on mitochondria was observed in the presence of GFP–OPTN and
326 mRuby–Ub (Fig. EV5B). In contrast, only very faint signals of phosphorylated TBK1 were
327 observed in the presence of nanobody–mRuby–Ub and GFP–OPTNΔUBAN (Fig. EV5B).
328 These data suggest that the fluidity of OPTN is also important for the feed-forward
329 mechanism between OPTN and TBK1 for the initiation of mitophagy. Together, we propose
330 that autophagy adaptors phase separate on ubiquitinated mitochondria to amplify the
331 initiation signals and wet the ATG9 vesicles to facilitate efficient mitophagy.

332 **Discussion**

333

334 **LLPS by autophagy adaptors during Parkin-mediated mitophagy**

335 In the present study, we discovered that autophagy adaptors accumulate on ubiquitinated
336 mitochondria with non-stoichiometric distribution compared with ubiquitin signals. They
337 displayed characteristics consistent with phase-separated structures, including dynamic
338 exchange with cytosol and redistribution upon coalescence. Notably, we observed the
339 enrichment of OPTN at the isolation membrane-positive region, which expanded along with
340 the elongation of the isolation membrane. These findings suggest that phase-separated
341 adaptors facilitate the effective engulfment of mitochondria by the isolation membrane
342 through the wetting effect and capillary forces (Fig. 6E, right panel). Moreover, the fluidity of
343 OPTN condensates is critical for the localization of ATG9 vesicles onto ubiquitinated
344 mitochondria, indicating that partial or complete wetting of phase-separated adaptors to
345 ATG9 vesicles may be crucial for their recruitment to and/or retention on mitochondria (Fig.
346 6E, left panel). Therefore, we propose that LLPS of autophagy adaptors plays a critical role
347 in two distinct steps of mitophagy by producing capillary forces, first, at the initiation step by
348 recruiting and retaining the ATG9 vesicles in the condensates and, second, at the
349 autophagosome elongation step by facilitating the attachment between ubiquitinated
350 mitochondria and the isolation membrane. Additionally, our experimental data suggest that
351 NDP52 also exhibits liquid-like properties. Further studies are needed to determine whether
352 condensate formation is necessary for mitophagy induction by NDP52.

353

354 **LLPS in bulk and selective autophagy**

355 Recent reports have shed light on the importance of LLPS in selective autophagy (Noda *et*
356 *al*, 2020). In lysophagy, p62 undergoes LLPS on lysosomes to facilitate efficient lysophagy
357 together with HSP27, which maintains the fluidity of p62 and prevents its gelation
358 (Gallagher & Holzbaur, 2023). This may also be mediated by the wetting between damaged
359 lysosomes and the isolation membrane by phase-separated p62. Indeed, p62 itself forms

360 phase-separated condensates along with ubiquitinated proteins, producing capillary forces
361 by the wetting effect to facilitate the engulfment by the isolation membrane (Agudo-
362 Canalejo *et al*, 2021). In our study, p62 exhibited low mobility, as determined by FRAP and
363 1,6-hexanediol experiments (Fig. 2B and EV2A). While these data may suggest that p62 is
364 immobile, they appear to contradict the observed redistribution of p62 to the area between
365 mitochondria upon clustering (Fig. EV1A and B). Thus, we speculate that p62 may exhibit
366 some degree of fluidity despite its low exchange between the condensate and cytosol.
367 Similarly to p62, Ape1, the cargo of the cytosol-to-vacuole targeting (Cvt) pathway in yeast,
368 forms gel-like condensates with Atg19 on the surface of Ape1 condensates to be
369 sequestered by the isolation membrane (Yamasaki *et al*, 2020). This association could also
370 be mediated by partial wetting. These examples together with our observations highlight
371 the importance of LLPS and the wetting phenomena in various selective autophagy
372 processes.

373 LLPS may also be important for non-selective bulk autophagy. In yeast, the Atg1
374 complex (the ULK1 complex in mammals) forms pre-autophagosomal structures (PASs),
375 which have been shown to be condensates driven by LLPS (Fujioka *et al*, 2020). Phase
376 separation in this context provides a high local concentration of the Atg1 complex to
377 support the autoactivation of Atg1 kinase (Yamamoto *et al*, 2016). Mammalian autophagy
378 factors also accumulate at the autophagosome formation site; FIP200, a subunit of the
379 autophagy-initiation complex, undergoes LLPS triggered by calcium transients (Zheng *et al*,
380 2022). The liquid-like nature of these autophagy-initiating structures may also be important
381 for the recruitment of Atg9/ATG9 vesicles through the wetting effect.

382

383 **The importance of phase separation during mitophagy**

384 In contrast to Parkin-mediated mitophagy, hypoxia-induced mitophagy does not involve
385 autophagy adaptors, and instead, the outer mitochondrial membrane proteins NIX (also
386 known as BNIP3L) and BNIP3 directly interact with ATG8 homologs on the isolation
387 membrane (Novak *et al*, 2010; Onishi *et al*, 2021). In this context, ATG8 proteins interact

388 with NIX or BNIP3, likely in a one-to-one manner. This raises the question of why phase
389 separation of autophagy adaptors is essential for Parkin-mediated mitophagy. One
390 possibility is that the quick induction and execution of Parkin-mediated mitophagy requires
391 amplification of the reactions through increased local concentration of adaptors and
392 autophagy-related proteins facilitated by LLPS. This is consistent with the fact that
393 mitophagy-inducing signals are also amplified by a mechanism involving phosphorylated
394 ubiquitin (Kane *et al*, 2014; Kazlauskaite *et al*, 2014; Koyano *et al*, 2014) and OPTN-TBK1
395 axis (Nguyen *et al*, 2023; Yamano *et al*, 2024). Indeed, we observed that the amount of
396 OPTN recruited to mitochondria was greater with wild-type OPTN than with OPTNΔUBAN
397 (in the presence of nanobody-Ub), likely reflecting the enhanced recruitment by condensate
398 formation (the reduced recruitment of OPTNΔUBAN may also be due to a lower expression
399 level of nanobody–mRuby–Ub compared to abundant endogenous ubiquitin, which may
400 further contribute to reduced mitophagy activity) (Fig. 5A and EV4A). Alternatively, Parkin-
401 mediated mitophagy requires a high level of precision and selectivity; mitophagy should be
402 induced only for damaged mitochondria, which is ensured by the recruitment and retention
403 of ATG9 vesicles only on phase-separated adaptor-positive mitochondria. This strict
404 specificity would enable proper quality control of the mitochondria.

405

406 **Materials and Methods**

407

408 **Cell culture and generation of stable cell lines**

409 HeLa cells, HeLa penta-knockout (penta KO) cells, and human embryonic kidney (HEK)
410 293T cells authenticated by RIKEN were cultured in Dulbecco's modified Eagle's medium
411 (DMEM; D6546; Sigma-Aldrich) supplemented with 10% fetal bovine serum (FBS; 173012;
412 Sigma-Aldrich) and 2 mM L-glutamine (25030-081; Gibco) in a 5% CO₂ incubator at 37°C.
413 For stable expression, retrovirus was produced with HEK293T cells transfected with pMRX-
414 IP-based, pMRX-IB-based, pMRX-IU-based, or pMRX-IN-based retroviral plasmids, pCG-
415 VSV-G, and pCG-gag-pol by using Lipofectamine 2000 (11668019; Thermo Fisher
416 Scientific). After transfection, cells were further incubated at 37°C for 24h. The viral
417 supernatant was collected by filtration through a 0.45-μm filter unit (Ultrafree-MC; Millipore)
418 and then used for infection. Cells were plated onto 6-cm dishes 18 h before infection, and
419 the medium was replaced with viral supernatant diluted 1.5-fold with 8 μg/mL polybrene
420 (H9268; Sigma-Aldrich). Two days later, cells were selected in a medium containing 2
421 μg/mL puromycin (P8833; Sigma-Aldrich), 4 μg/mL blasticidin S hydrochloride (022-18713;
422 FUJIFILM Wako Pure Chemical Corporation), 1.5 mg/mL neomycin, or 250 μg/mL zeocin
423 (R25005; Thermo Fisher Scientific).

424

425 **Plasmids**

426 The pMRX-IPU, pMRX-IBU and pMRX-INU plasmids were generated by modifying the
427 multi-cloning site of pMRX-IP (Saitoh *et al*, 2002; Kitamura *et al*, 2003), pMRX-IB, and
428 pMRX-IN, respectively. DNA fragments encoding ubiquitin, p62 (NM_003900.5), OPTN
429 (NM_001008211.1), NBR1 (NM_001291571.2), NDP52 (NM_001261391.2), TAX1BP1
430 (NM_001206901.1), ATG9A (NM_001077198.3), LC3A (NM_032514.4), and LC3B
431 (NM_022818.5) were inserted into pMRX-IPU, pMRX-INU, or pMRX-IBU. DNAs encoding
432 the HA epitope, monomeric enhanced GFP with the A206K mutation (mGFP), codon-
433 optimized ultra-stable GFP (muGFP) (Scott *et al*, 2018), codon-optimized mRuby3 (Bajar *et*

434 *et al.*, 2016), HaloTag7 (G1891; Promega), 3×FLAG, and SNAP-tag (New England BioLabs,
435 N9181S) were used for tagging. The mitochondrial presequence of *Neurospora crassa* Fo-
436 ATPase subunit 9 (residues 1–69) was added to HaloTag7-SNAP to deliver the reporter into
437 the mitochondrial matrix (mtHalo-SNAP) (Eura, 2003). Truncated OPTN (OPTNΔUBAN, aa
438 445–502) was prepared by PCR-mediated site-directed mutagenesis. The resulting
439 plasmids were sequenced.

440

441 **Antibodies and reagents**

442 The primary antibodies used in this study were rabbit polyclonal anti-OPTN (Proteintech,
443 10837-AP), rabbit polyclonal anti-ATG9A (MBL, PD042), mouse monoclonal anti-Halo
444 (Promega, G9211), mouse monoclonal anti-HSP90 (BD Transduction Laboratories,
445 610419), rabbit polyclonal anti-GFP (Thermo Fisher Scientific, A6455), rabbit polyclonal
446 anti-NDP52 (Proteintech, 12229-1-AP), rabbit polyclonal anti-RB1CC1 (Proteintech, 17250-
447 1-AP), and rabbit monoclonal anti-phospho-TBK1 (Ser172) (Cell Signaling Technology,
448 5483) antibodies. The secondary antibodies used were HRP-conjugated goat polyclonal
449 anti-rabbit IgG (Jackson ImmunoResearch Laboratories, 111-035-144) and HRP-
450 conjugated goat polyclonal anti-mouse IgG (Jackson ImmunoResearch Laboratories, 115-
451 035-003) antibodies. To induce mitophagy, HeLa cells were treated with 20 μM carbonyl
452 cyanide *m*-chlorophenyl hydrazine (CCCP; Sigma-Aldrich) for 45 min, or 10 μM oligomycin
453 (Cabiotech, 495455-10MGCN) and 4 μM antimycin A (Sigma-Aldrich, A8674) for 18 h.
454 After cells had been treated with oligomycin and antimycin A for >6 h, 10 μM Q-VD-OPH
455 (SM Biochemicals, SMPH001) was added to block apoptotic cell death. To inhibit the
456 formation of isolation membranes in the 1,6-hexanediol (Sigma-Aldrich, 240117-50G)
457 treatment experiment, wortmannin (Sigma-Aldrich, W1628-1MG) was added into the
458 medium.

459

460 **Immunoprecipitation and immunoblotting**

461 Cell lysates were prepared in a lysis buffer (50 mM Tris-HCl pH 7.4, 150 mM NaCl, 1 mM

462 EDTA, 1% Triton X-100, EDTA-free protease inhibitor cocktail [19543200; Roche]). After
463 centrifugation at 17,700 × g for 10 min, the supernatants were subjected to
464 immunoprecipitation using anti-FLAG M2 magnetic beads (M8823-1ML; Sigma-Aldrich).
465 Precipitated immunocomplexes were washed three times with lysis buffer and boiled in
466 sample buffer (46.7 mM Tris-HCl, pH 6.8, 5% glycerol, 1.67% sodium dodecyl sulfate,
467 1.55% dithiothreitol, and 0.02% bromophenol blue). For immunoprecipitation of ATG9
468 vesicles, cells were disrupted by Dounce homogenization with hypotonic lysis buffer (10
469 mM HEPES, pH 7.9, 1.5 mM MgCl₂ and 10 mM KCl, EDTA-free protease inhibitor cocktail
470 [19543200; Roche]). Disruption was carried out by applying 35 strokes while the cell
471 suspension was cooled on ice. The supernatants were subjected to immunoprecipitation
472 using anti-FLAG M2 magnetic beads (M8823-1ML; Sigma-Aldrich). For immunoblotting, the
473 samples were separated by SDS-PAGE and transferred to Immobilon-P polyvinylidene
474 difluoride membranes (Millipore, WBKLS0500) with the Trans-Blot Turbo Transfer System
475 (Bio-Rad). After incubation with the relevant antibody in 5% skim milk in 20 mM Tris-HCl,
476 150 mM NaCl, and 0.1% Tween 20 (02194841-CF; MP Biomedicals), the signals from
477 incubation with SuperSignal West Pico Chemiluminescent Substrate (Thermo Fisher
478 Scientific, 34579) were detected with the FUSION SOLO.7S.EDGE imaging system (Vilber-
479 Lourmat). Contrast and brightness adjustment and quantification were performed using the
480 image processing software Fiji (Schindelin *et al*, 2012).

481

482 **Fluorescence recovery after photobleaching**

483 In-cell fluorescence recovery after photobleaching (FRAP) analyses were performed with
484 an Olympus Fluoview FV3000 confocal microscope equipped with a 60× oil-immersion
485 objective lens (1.40 NA, Olympus). The chamber was maintained at 37°C and continuously
486 supplied with humidified 5% CO₂. Bleaching was performed using 80% laser power (488 or
487 561 nm laser), and images were captured every 5 s for 30 frames. Recovery curves and
488 fitting were analyzed using OriginPro 2022. Fluorescence intensity of the bleached spot, an
489 unbleached control spot, and the background was measured using the software package

490 Fiji. Background intensity was subtracted, and the intensity values of the region of interest
491 are reported relative to the pre-bleached images during image acquisition. Each data point
492 represents the mean and standard error of fluorescence intensities in more than three
493 unbleached (control) or bleached (experimental) spots.

494

495 **Live-cell imaging**

496 Living imaging was conducted with the Olympus SpinSR10 spinning-disk confocal super-
497 resolution microscope equipped with a Hamamatsu ORCA-Flash 4.0 camera, a UPLAPO
498 OHR 100 × (NA 1.50) lens, and the SORA disk in place. The microscope was operated with
499 Olympus cellSens Dimension 2.3 software. Cells were passaged onto a four-chamber
500 glass-bottom dish (Greiner Bio-One) more than 24 h before imaging. To induce mitophagy,
501 cells were incubated with 10 µM CCCP in the presence of 200 nM SF650-conjugated Halo
502 ligand (GoryoChemical, A308-02). Images were processed using the image processing
503 software package Fiji (Schindelin *et al*, 2012). Fluorescence intensity of indicated
504 fluorophores was measured by Fiji, and spline connected graphs were created using
505 OriginPro 2022 software.

506

507 **Immunofluorescence imaging**

508 Cells were fixed with 4% PFA in 0.1 M phosphate buffer (pH 7.3) for 15 min at room
509 temperature (RT) and washed with PBS. Fixed cells were incubated with 10 µg/mL digitonin
510 for 5 min at RT and washed with PBS. Then, cells were incubated with primary antibodies
511 diluted (1:1000) in blocking buffer (3% BSA, in PBS) for 1 h at RT, washed with PBS,
512 incubated with Alexa Fluor-conjugated secondary antibodies (1:1000) in blocking buffer for
513 60 min at RT, washed again, and mounted on coverslips. Colocalization was calculated by
514 Fiji plugins BIOP JACoP, with the threshold of the ATG9A channel fixed to 500. ATG9A-
515 positive areas out of GFP-positive areas were calculated to obtain the overlapping areas.

516

517 **Mathematical model of autophagy adaptor condensate formation**

518 We formulated a mathematical model of autophagy adaptor condensate formation. For the
 519 case of two mitochondria approaching each other (Fig. 3A), the free energy, F , of the
 520 system can be written as

$$F = \int (f_{int} + f_{ent}) dV, \#(1)$$

521 with the interaction energy, f_{int} , and the entropic energy, f_{ent} , expressed as

$$f_{int} = \frac{\sigma}{2} (\nabla \phi_{ad})^2 - \chi_{self} \phi_{ad}^2 - \chi_{Ub} \phi_{Ub} \phi_{ad} + \chi_{Mt} \phi_{Mt} \phi_{ad}, \#(2)$$

$$f_{ent} = \phi_{ad} \ln \phi_{ad} + \phi_{sol} \ln \phi_{sol}, \#(3)$$

522 where ϕ_{ad} , ϕ_{Ub} , and $\phi_{sol} = 1 - \phi_{ad} - \phi_{Ub} - \phi_{Mt}$ are the adaptor, ubiquitin, and solvent
 523 concentrations, respectively, χ_{self} and χ_{Ub} represent the strength of the adaptor self-
 524 interaction and adaptor–ubiquitin interaction, respectively, σ represents the surface tension
 525 of the condensates, and χ_{Mt} represents the mitochondrial area exclusion effect, introduced
 526 to prevent proteins from entering the mitochondrial interior (ϕ_{Mt}).

527 For the case in which an isolation membrane surrounded a mitochondrion (Fig. 3C),
 528 the interaction energy, f_{int} , is instead expressed as

$$f_{int} = \frac{\sigma}{2} (\nabla \phi_{ad})^2 - \chi_{self} \phi_{ad}^2 - \chi_{Ub} \phi_{Ub} \phi_{ad} - \chi_{LC3} \phi_{LC3} \phi_{ad} + \chi_{Mt} \phi_{Mt} \phi_{ad} + \chi_{IM} \phi_{IM} \phi_{ad}, \#(5)$$

529 where ϕ_{LC3} and χ_{LC3} represent the LC3 concentrations and the strength of the adaptor–LC3
 530 interaction, respectively, and χ_{IM} represents the mitochondrial area exclusion effect,
 531 introduced to prevent proteins from entering the lumen of the isolation membrane (ϕ_{IM}).

532 The solvent concentration that appears in the entropic energy (3) was also modified to
 533 $\phi_{sol} = 1 - \phi_{ad} - \phi_{Ub} - \phi_{LC3} - \phi_{Mt} - \phi_{IM}$.

534 For the numerical simulation, the space was discretized by a lattice with 10 nm on
 535 each side, and a concentration field was assigned to each location. The time evolution of
 536 the system was assumed to follow the Cahn–Hilliard equation,

$$\frac{\partial \phi_{ad}}{\partial t} = \frac{\partial}{\partial \vec{x}} \left[M \frac{\partial}{\partial \vec{x}} \left(\frac{\delta F}{\delta \phi_{ad}} \right) \right], \#(4)$$

537 which is commonly used in analyses of phase separation dynamics (Berry *et al.*, 2018).
 538 Here, $M = D/k_B T$ is the mobility of the protein with the diffusion constant $D = 10 \mu\text{m}^2/\text{sec}$
 539 (Milo & Phillips, 2015) expressed in terms of the Boltzmann constant k_B and temperature T .

540 We considered a 3000 nm × 3000 nm square region with periodic boundary conditions
541 containing two mitochondria and surrounding cytosolic components as a system and
542 assumed that adaptor proteins are uniformly distributed in the cytosol around mitochondria
543 at a concentration of $\phi = 0.1$ in the initial state.

544

545 **Statistical analysis**

546 Statistical analysis was performed using OriginPro 2022 software. The statistical methods
547 used for each analysis are specified in the figure legends. No sample size calculation was
548 performed, the experiments were not randomized, and investigators were not blinded
549 during experiments.

550

551 **Data Availability**

552 This study includes no data deposited in external repositories.

553

554 **Acknowledgments**

555 We thank Michael Lazarou (Walter and Eliza Hall Institute of Medical Research) for
556 providing pentaKO HeLa cells, Toshio Kitamura for pMXs-IP (The University of Tokyo),
557 Shoji Yamaoka (Tokyo Medical and Dental University, Tokyo, Japan) for pMRXIP, and
558 Teruhito Yasui (National Institutes of Biomedical Innovation, Health and Nutrition
559 (NIBIOHN), Osaka, Japan) for pCG-VSV-G and pCG-gag-pol. pKanCMV-mClover3-
560 mRuby3 was a gift from Michael Lin (Addgene plasmid # 74252 ;
561 <http://n2t.net/addgene:74252> ; RRID: Addgene_74252).

562 This work was supported by the Exploratory Research for Advanced Technology (ERATO)
563 research funding program of the Japan Science and Technology Agency (JST)
564 (JPMJER1702 to NM), a Grant-in-Aid for Specially Promoted Research (22H04919 to NM)
565 and a Grant-in-Aid for Scientific Research (C) (23K05715 to Y.S.) from the Japan Society
566 for the Promotion of Science (JSPS), World Research Hub (WRH) Program of the
567 International Research Frontiers Initiative, Tokyo Institute of Technology (RLK), and

568 German Research Foundation (Project 460056461 to RLK). The numerical computations
569 have been performed with the RIKEN supercomputer system (HOKUSAI).

570

571 **Disclosure and competing interests statement**

572 The authors declare that they have no conflict of interest.

573

574 **References**

- 575 Agudo-Canalejo J, Schultz SW, Chino H, Migliano SM, Saito C, Koyama-Honda I,
576 Stenmark H, Brech A, May AI, Mizushima N, *et al* (2021) Wetting regulates autophagy
577 of phase-separated compartments and the cytosol. *Nature* 591: 142–146
- 578 Bajar BT, Wang ES, Lam AJ, Kim BB, Jacobs CL, Howe ES, Davidson MW, Lin MZ & Chu J
579 (2016) Improving brightness and photostability of green and red fluorescent proteins
580 for live cell imaging and FRET reporting. *Sci Rep* 6: 20889
- 581 Berry J, Brangwynne CP & Haataja M (2018) Physical principles of intracellular
582 organization via active and passive phase transitions. *Reports on Progress in Physics*
583 81: 046601
- 584 Eura Y (2003) Two Mitofusin Proteins, Mammalian Homologues of FZO, with Distinct
585 Functions Are Both Required for Mitochondrial Fusion. *J Biochem* 134: 333–344
- 586 Fujioka Y, Alam JM, Noshiro D, Mouri K, Ando T, Okada Y, May AI, Knorr RL, Suzuki K,
587 Ohsumi Y, *et al* (2020) Phase separation organizes the site of autophagosome
588 formation. *Nature* 578: 301–305
- 589 Gallagher ER & Holzbaur ELF (2023) The selective autophagy adaptor p62/SQSTM1 forms
590 phase condensates regulated by HSP27 that facilitate the clearance of damaged
591 lysosomes via lysophagy. *Cell Rep* 42: 112037
- 592 Ganley IG & Simonsen A (2022) Diversity of mitophagy pathways at a glance. *J Cell Sci*
593 135: jcs259748
- 594 Geisler S, Holmström KM, Skujat D, Fiesel FC, Rothfuss OC, Kahle PJ & Springer W
595 (2010) PINK1/Parkin-mediated mitophagy is dependent on VDAC1 and p62/SQSTM1.
596 *Nat Cell Biol* 12: 119–131
- 597 Gouveia B, Kim Y, Shaevitz JW, Petry S, Stone HA & Brangwynne CP (2022) Capillary
598 forces generated by biomolecular condensates. *Nature* 609: 255–264
- 599 Gubas A & Dikic I (2022) A guide to the regulation of selective autophagy receptors. *FEBS*
600 *J* 289: 75–89
- 601 Heo J-M, Ordureau A, Paulo JA, Rinehart J & Harper JW (2015) The PINK1-PARKIN
602 Mitochondrial Ubiquitylation Pathway Drives a Program of OPTN/NDP52 Recruitment
603 and TBK1 Activation to Promote Mitophagy. *Mol Cell* 60: 7–20
- 604 Hirose T, Ninomiya K, Nakagawa S & Yamazaki T (2023) A guide to membraneless
605 organelles and their various roles in gene regulation. *Nat Rev Mol Cell Biol* 24: 288–
606 304
- 607 Hyman AA, Weber CA & Jülicher F (2014) Liquid-Liquid Phase Separation in Biology. *Annu*
608 *Rev Cell Dev Biol* 30: 39–58
- 609 Itakura E, Kishi-Itakura C, Koyama-Honda I & Mizushima N (2012) Structures containing
610 Atg9A and the ULK1 complex independently target depolarized mitochondria at initial
611 stages of Parkin-mediated mitophagy. *J Cell Sci* 125: 1488–1499
- 612 Kane LA, Lazarou M, Fogel AI, Li Y, Yamano K, Sarraf SA, Banerjee S & Youle RJ (2014)
613 PINK1 phosphorylates ubiquitin to activate Parkin E3 ubiquitin ligase activity. *Journal*
614 *of Cell Biology* 205: 143–153

- 615 Kazlauskaitė A, Kondapalli C, Gourlay R, Campbell DG, Ritorto MS, Hofmann K, Alessi DR,
616 Knebel A, Trost M & Muqit MMK (2014) Parkin is activated by PINK1-dependent
617 phosphorylation of ubiquitin at Ser65. *Biochemical Journal* 460: 127–141
- 618 Kitamura T, Koshino Y, Shibata F, Oki T, Nakajima H, Nosaka T & Kumagai H (2003)
619 Retrovirus-mediated gene transfer and expression cloning: powerful tools in functional
620 genomics. *Exp Hematol* 31: 1007–1014
- 621 Koyano F, Okatsu K, Kosako H, Tamura Y, Go E, Kimura M, Kimura Y, Tsuchiya H,
622 Yoshihara H, Hirokawa T, et al (2014) Ubiquitin is phosphorylated by PINK1 to activate
623 parkin. *Nature* 510: 162–166
- 624 Kusumaatmaja H, May AI, Feeney M, McKenna JF, Mizushima N, Frigerio L & Knorr RL
625 (2021a) Wetting of phase-separated droplets on plant vacuole membranes leads to a
626 competition between tonoplast budding and nanotube formation. *Proceedings of the
627 National Academy of Sciences* 118: e2024109118
- 628 Kusumaatmaja H, May AI & Knorr RL (2021b) Intracellular wetting mediates contacts
629 between liquid compartments and membrane-bound organelles. *J Cell Biol* 220:
630 e202103175
- 631 Lamark T & Johansen T (2021) Mechanisms of Selective Autophagy. *Annu Rev Cell Dev
632 Biol* 37: 143–169
- 633 Lazarou M, Sliter DA, Kane LA, Sarraf SA, Wang C, Burman JL, Sideris DP, Fogel AI &
634 Youle RJ (2015) The ubiquitin kinase PINK1 recruits autophagy receptors to induce
635 mitophagy. *Nature* 524: 309–314
- 636 Li F, Xu D, Wang Y, Zhou Z, Liu J, Hu S, Gong Y, Yuan J & Pan L (2018) Structural insights
637 into the ubiquitin recognition by OPTN (optineurin) and its regulation by TBK1-
638 mediated phosphorylation. *Autophagy* 14: 66–79
- 639 Ma X, Li P & Ge L (2023) Targeting of biomolecular condensates to the autophagy pathway.
640 *Trends Cell Biol* 33: 505–516
- 641 Mangiarotti A, Chen N, Zhao Z, Lipowsky R & Dimova R (2023) Wetting and complex
642 remodeling of membranes by biomolecular condensates. *Nat Commun* 14: 2809
- 643 McSwiggen DT, Mir M, Darzacq X & Tjian R (2019) Evaluating phase separation in live
644 cells: diagnosis, caveats, and functional consequences. *Genes Dev* 33: 1619–1634
- 645 Milo R & Phillips R (2015) Cell Biology by the Numbers Garland Science
- 646 Milovanovic D & De Camilli P (2017) Synaptic Vesicle Clusters at Synapses: A Distinct
647 Liquid Phase? *Neuron* 93: 995–1002
- 648 Mizushima N & Levine B (2020) Autophagy in Human Diseases. *New England Journal of
649 Medicine* 383: 1564–1576
- 650 Moore AS & Holzbaur ELF (2016) Dynamic recruitment and activation of ALS-associated
651 TBK1 with its target optineurin are required for efficient mitophagy. *Proceedings of the
652 National Academy of Sciences* 113: E3349–E3358
- 653 Musacchio A (2022) On the role of phase separation in the biogenesis of membraneless
654 compartments. *EMBO J* 41: e109952
- 655 Nakatogawa H (2020) Mechanisms governing autophagosome biogenesis. *Nat Rev Mol
656 Cell Biol* 21: 439–458

- 657 Narendra DP, Kane LA, Hauser DN, Fearnley IM & Youle RJ (2010) p62/SQSTM1 is
658 required for Parkin-induced mitochondrial clustering but not mitophagy; VDAC1 is
659 dispensable for both. *Autophagy* 6: 1090–1106
- 660 Nguyen TN, Sawa-Makarska J, Khuu G, Lam WK, Adriaenssens E, Fracchiolla D,
661 Shoebridge S, Bernklau D, Padman BS, Skulsupaisarn M, et al (2023)
662 Unconventional initiation of PINK1/Parkin mitophagy by Optineurin. *Mol Cell* 83: 1693–
663 1709.e9
- 664 Noda NN, Wang Z & Zhang H (2020) Liquid–liquid phase separation in autophagy. *Journal
665 of Cell Biology* 219: e202004062
- 666 Novak I, Kirkin V, McEwan DG, Zhang J, Wild P, Rozenknop A, Rogov V, Löhr F, Popovic D,
667 Occhipinti A, et al (2010) Nix is a selective autophagy receptor for mitochondrial
668 clearance. *EMBO Rep* 11: 45–51
- 669 Okatsu K, Saisho K, Shimanuki M, Nakada K, Shitara H, Sou YS, Kimura M, Sato S,
670 Hattori N, Komatsu M, et al (2010) P62/SQSTM1 cooperates with Parkin for
671 perinuclear clustering of depolarized mitochondria. *Genes to Cells* 15: 887–900
- 672 O'Loughlin T, Kruppa AJ, Ribeiro ALR, Edgar JR, Ghannam A, Smith AM & Buss F (2020)
673 OPTN recruitment to a Golgi-proximal compartment regulates immune signalling and
674 cytokine secretion. *J Cell Sci* 133: 1–15
- 675 Onishi M, Yamano K, Sato M, Matsuda N & Okamoto K (2021) Molecular mechanisms and
676 physiological functions of mitophagy. *EMBO J* 40: e104705
- 677 Park D, Wu Y, Wang X, Gowrishankar S, Baublis A & De Camilli P (2023) Synaptic vesicle
678 proteins and ATG9A self-organize in distinct vesicle phases within synapsin
679 condensates. *Nat Commun* 14: 455
- 680 Peng S, Chen X-H, Chen S, Zhang J, Wang C, Liu W, Zhang D, Su Y & Zhang X (2021)
681 Phase separation of Nur77 mediates celastrol-induced mitophagy by promoting the
682 fluidity of p62/SQSTM1 condensates. *Nat Commun* 12: 5989
- 683 Rothbauer U, Zolghadr K, Muyldermans S, Schepers A, Cardoso MC & Leonhardt H (2008)
684 A Versatile Nanotrap for Biochemical and Functional Studies with Fluorescent Fusion
685 Proteins. *Molecular & Cellular Proteomics* 7: 282–289
- 686 Saitoh T, Nakano H, Yamamoto N & Yamaoka S (2002) Lymphotoxin-beta receptor
687 mediates NEMO-independent NF-kappaB activation. *FEBS Lett* 532: 45–51
- 688 Sansevino R, Hoffmann C & Milovanovic D (2023) Condensate biology of synaptic vesicle
689 clusters. *Trends Neurosci* 46: 293–306
- 690 Schindelin J, Arganda-Carreras I, Frise E, Kaynig V, Longair M, Pietzsch T, Preibisch S,
691 Rueden C, Saalfeld S, Schmid B, et al (2012) Fiji: an open-source platform for
692 biological-image analysis. *Nat Methods* 9: 676–682
- 693 Scott DJ, Gunn NJ, Yong KJ, Wimmer VC, Veldhuis NA, Challis LM, Haidar M, Petrou S,
694 Bathgate RAD & Griffin MDW (2018) A Novel Ultra-Stable, Monomeric Green
695 Fluorescent Protein For Direct Volumetric Imaging of Whole Organs Using CLARITY.
696 *Sci Rep* 8: 667
- 697 Style RW, Jagota A, Hui C-Y & Dufresne ER (2017) Elastocapillarity: Surface Tension and
698 the Mechanics of Soft Solids. *Annu Rev Condens Matter Phys* 8: 99–118

- 699 Sun D, Wu R, Zheng J, Li P & Yu L (2018) Polyubiquitin chain-induced p62 phase
700 separation drives autophagic cargo segregation. *Cell Res* 28: 405–415
- 701 Taylor NO, Wei M-T, Stone HA & Brangwynne CP (2019) Quantifying Dynamics in Phase-
702 Separated Condensates Using Fluorescence Recovery after Photobleaching. *Biophys
J* 117: 1285–1300
- 703
- 704 Turco E, Savova A, Gere F, Ferrari L, Romanov J, Schuschnig M & Martens S (2021)
705 Reconstitution defines the roles of p62, NBR1 and TAX1BP1 in ubiquitin condensate
706 formation and autophagy initiation. *Nat Commun* 12: 5212
- 707 Vargas JNS, Hamasaki M, Kawabata T, Youle RJ & Yoshimori T (2023) The mechanisms
708 and roles of selective autophagy in mammals. *Nat Rev Mol Cell Biol* 24: 167–185
- 709 Wexler JS, Heard TM & Stone HA (2014) Capillary Bridges between Soft Substrates. *Phys
Rev Lett* 112: 066102
- 710
- 711 Wong YC & Holzbaur ELF (2014) Optineurin is an autophagy receptor for damaged
712 mitochondria in parkin-mediated mitophagy that is disrupted by an ALS-linked
713 mutation. *Proceedings of the National Academy of Sciences* 111: E4439–E4448
- 714 Yamamoto H, Fujioka Y, Suzuki SW, Noshiro D, Suzuki H, Kondo-Kakuta C, Kimura Y,
715 Hirano H, Ando T, Noda NN, et al (2016) The Intrinsically Disordered Protein Atg13
716 Mediates Supramolecular Assembly of Autophagy Initiation Complexes. *Dev Cell* 38:
717 86–99
- 718 Yamamoto H, Kakuta S, Watanabe TM, Kitamura A, Sekito T, Kondo-Kakuta C, Ichikawa R,
719 Kinjo M & Ohsumi Y (2012) Atg9 vesicles are an important membrane source during
720 early steps of autophagosome formation. *Journal of Cell Biology* 198: 219–233
- 721 Yamano K, Kikuchi R, Kojima W, Hayashida R, Koyano F, Kawawaki J, Shoda T, Demizu Y,
722 Naito M, Tanaka K, et al (2020) Critical role of mitochondrial ubiquitination and the
723 OPTN-ATG9A axis in mitophagy. *J Cell Biol* 219: e201912144
- 724 Yamano K, Sawada M, Kikuchi R, Nagataki K, Kojima W, Endo R, Kinoshita H, Sugihara A,
725 Fujino T, Watanabe A, et al (2024) Optineurin provides a mitophagy contact site for
726 TBK1 activation. *EMBO J* 43: 754–779
- 727 Yamasaki A, Alam JM, Noshiro D, Hirata E, Fujioka Y, Suzuki K, Ohsumi Y & Noda NN
728 (2020) Fluidity Is a Critical Determinant for Selective Autophagy of Protein
729 Condensates. *Mol Cell* 77: 1163–1175.e9
- 730 Yim WW-Y, Yamamoto H & Mizushima N (2022) A pulse-chase reporter processing
731 assay for mammalian autophagic flux with HaloTag. *Elife* 11: e78923
- 732 Zaffagnini G, Savova A, Danieli A, Romanov J, Tremel S, Ebner M, Peterbauer T, Sztach
733 M, Trapannone R, Tarafder AK, et al (2018) p62 filaments capture and present
734 ubiquitinated cargos for autophagy. *EMBO J* 37: e98308
- 735 Zheng Q, Chen Y, Chen D, Zhao H, Feng Y, Meng Q, Zhao Y & Zhang H (2022) Calcium
736 transients on the ER surface trigger liquid-liquid phase separation of FIP200 to specify
737 autophagosome initiation sites. *Cell* 185: 4082–4098.e22
- 738
- 739

740 **Figure legends**

741

742 **Figure 1. Autophagy adaptors show distinct distributions during Parkin-mediated**
743 **mitophagy.**

744 (A and B) Representative images (left) and spline graphs of the intensity profiles along the
745 indicated arrows (from position 0) in the respective images (right) of wild-type HeLa cells
746 expressing one of the GFP-tagged autophagy adaptors or ubiquitin, mRuby–Omp25, and
747 HaloTag7–LC3B at 45 min after CCCP treatment. Separate mitochondria without contacting
748 other mitochondria or isolation membranes (A; Mt) or mitochondria with an isolation
749 membrane (B; Mt–IM) are shown. The y-axis in each of the graphs indicates the
750 fluorescence intensity. Scale bars indicate 1 μ m.

751 (C) The relative intensity of GFP-tagged adaptors or ubiquitin (a and b) in LC3B-positive
752 areas compared with LC3B-negative areas in panel B. GFP signals were normalized to the
753 mRuby–Omp25 signals (a' and b') using the formula Relative Intensity = $(a/b)/(a'/b')$, where
754 a and a' represent the intensities in the LC3B-positive area, and b and b' represent the
755 intensities in the LC3B-negative area. Solid horizontal bars indicate the means, and dots
756 indicate the data from five structures. Differences were statistically analyzed by one-way
757 analysis of variance with Dunnett's post-hoc test.

758 (D) Immunostaining of endogenous OPTN or NDP52 in wild-type HeLa cells expressing
759 mRuby–Omp25 and HaloTag7–LC3B at 45 min after CCCP treatment. Scale bars indicate
760 4 μ m and 1 μ m (magnified images).

761 (E) Representative images (left) and spline graphs of the intensity profiles along the
762 indicated arrows (from position 0) in the respective images (right) of HeLa cells lacking all
763 five autophagy adaptors (penta KO cells) expressing indicated GFP-tagged autophagy
764 adaptors, mRuby–Omp25, and HaloTag7–LC3B at 45 min after CCCP treatment.
765 Mitochondria with an isolation membrane (Mt–IM) are shown. The y-axis in each of the
766 graphs indicates the fluorescence intensity. Scale bars indicate 1 μ m.

767 (F) The relative intensity of GFP-tagged adaptors or ubiquitin (a and b) in LC3B-positive

768 areas compared with LC3B-negative areas in panel E. Relative intensities were calculated
769 as in (C). Solid horizontal bars indicate the means, and dots indicate the data from five
770 structures. Differences were statistically analyzed by one-way analysis of variance with
771 Dunnett's post-hoc test.

772

773 **Figure 2. OPTN and NDP52 show a dynamic exchange between the mitochondrial**
774 **surface and cytosol.**

775 (A–D) Representative images (A and C) and quantification (B and D) of GFP fluorescence
776 recovery after photobleaching (FRAP) on separate mitochondria (Mt) (A and B) or on
777 mitochondria with an isolation membrane (Mt–IM) (C and D) in HeLa cells lacking all five
778 autophagy adaptors (penta KO cells) expressing GFP-tagged adaptors or ubiquitin at 45
779 min after CCCP treatment. The photobleached areas are indicated by dotted lines. The
780 magnified panels display time-lapse images of the photobleached areas. Scale bars
781 indicate 2 μ m and 1 μ m (magnified images). Data were collected from four structures and
782 were fitted to the equation $y = a*(1 - \exp(-b*x))$. The dark shaded areas represent the 95%
783 confidence intervals, and the light shaded areas represent the 95% prediction intervals.
784 (E) Penta KO cells expressing GFP–OPTN and GFP–NDP52 at 45 min after treatment with
785 CCCP and wortmannin. Wortmannin was added to inhibit autophagosome formation so that
786 OPTN is not sequestered in a closed compartment. Images of cells before (upper panels)
787 and 2 min after (lower panels) the addition of 10% 1,6-hexanediol are displayed. Scale
788 bars, 5 μ m and 2 μ m (magnified images).

789

790 **Figure 3. Mathematical models of condensate formation and localization of**
791 **autophagy adaptors.**

792 (A) Schematic diagram of two separated mitochondria.

793 (B) Sheet-like condensates of autophagy adaptors on mitochondria deform when the inter-
794 mitochondrial distance d_{Mt} was changed. The strength of adaptor self-interaction (χ_{self}),
795 adaptor–ubiquitin interaction (χ_{Ub}), mitochondrial area exclusion (χ_{Mt}) and surface tension

796 (σ) were set to $\chi_{self} = 3k_B T$, $\chi_{Ub} = 12k_B T$, $\chi_{Mt} = 5k_B T$, and $\sigma = k_B T$, respectively. The
797 color indicates the adaptor concentration (ϕ_{ad}). Arrowheads indicate autophagy adaptors
798 filling the cleft between the two mitochondria.

799 (C) Schematic diagram of a single mitochondrion with an isolation membrane.
800 (D) Sheet-like condensates of autophagy adaptors on mitochondria deformed when the
801 isolation membrane (arrowheads) appeared and the angle α surrounding the mitochondria
802 changed. The strength of adaptor self-interaction (χ_{self}), adaptor–ubiquitin interaction (χ_{Ub}),
803 adaptor–LC3 interaction (χ_{LC3}), mitochondrial area exclusion (χ_{Mt}), isolation membrane
804 area exclusion (χ_{IM}), and surface tension (σ) were set to $\chi_{self} = 3k_B T$, $\chi_{Ub} = \chi_{LC3} = 12k_B T$,
805 $\chi_{Mt} = \chi_{IM} = 5k_B T$, and $\sigma = k_B T$, respectively. The color indicates the adaptor
806 concentration (ϕ_{ad}).

807

808 **Figure 4. OPTN condensates redistribute upon contact with membranes.**

809 (A–D) Time-lapse images (A and C) and spline graphs (B and D) of two separate
810 mitochondria approaching and contacting each other. Events of the attachment of two
811 mitochondria with comparable sizes (A and B) and with differing sizes (C and D) were
812 observed. The line graphs represent the intensity profiles along the indicated arrows (from
813 position 0) in the respective images shown (B and D). The arrowheads indicate
814 redistributed OPTN signals filling the cleft between two adjacent mitochondria. Scale bars
815 indicate 1 μm . See also Movie EV1 for the time-lapse video corresponding to (C).
816 (E and F) Time-lapse images (E) and a spline graph (F) of a mitochondrion with an isolation
817 membrane elongating on its surface. The arrowhead indicates the elongating isolation
818 membrane. The line graph represent the intensity profiles along the indicated arrows (from
819 position 0) in the respective images shown. Scale bars indicate 1 μm . See also Movie EV2
820 for the time-lapse video corresponding to (E).

821

822 **Figure 5. Liquid-like property of OPTN condensates is required for mitophagy.**

823 (A) HeLa cells lacking all five autophagy adaptors (penta KO cells) expressing both GPF–

824 OPTN and mRuby–Ub (i), both GFP–OPTN and anti-GFP nanobody–mRuby–Ub (ii), both
825 GFP–OPTNΔUBAN and mRuby–Ub (iii), or both GFP–OPTNΔUBAN and anti-GFP
826 nanobody–mRuby–Ub (iv) at 45 min after CCCP treatment. Time-lapse images of GFP
827 FRAP are shown. Photobleached areas are circled by dotted lines. Scale bars indicate 4
828 μ m and 2 μ m (magnified images).

829 (B) Interaction between GFP–OPTN and OPTN mutants and FLAG–Ub or FLAG–
830 nanobody–Ub was investigated by immunoprecipitation with an anti-FLAG antibody and
831 immunoblotting with an anti-GFP antibody.

832 (C) Quantification of GFP FRAP on separate mitochondria (Mt) in penta KO cells
833 expressing both GFP–OPTN and mRuby–Ub (i; gray), both GFP–OPTN and anti-GFP
834 nanobody–mRuby–Ub (ii; red), or both GFP–OPTNΔUBAN and anti-GFP nanobody–
835 mRuby–Ub (iv; blue) at 45 min after CCCP treatment. Data were collected from four
836 structures and were fitted to the equation $y = a^*(1 - \exp(-b^*x))$. The dark shading
837 represents the 95% confidence intervals, and the light shading represents the 95%
838 prediction intervals.

839 (D and E) Representative data (D) and quantification (E) of HaloTag (Halo) processing
840 assay using cells expressing the indicated OPTN and Ub constructs. Cells expressing the
841 mtHalo–SNAP mitophagy reporter were treated without (0 h) and with oligomycin and
842 antimycin for 18 h. The amount of processed Halo (proc. Halo) indicates the relative
843 amount of mitochondria degraded in lysosomes. Solid horizontal bars indicate the means,
844 and dots indicate the data from at least three independent cultures. Differences were
845 statistically analyzed by one-way analysis of variance with Dunnett's post-hoc test.

846

847 **Figure 6. Liquid-like property of OPTN condensates is required for the recruitment of**
848 **ATG9 vesicles.**

849 (A and B) Localization of ATG9 vesicles under normal (CCCP–) or mitophagy-inducing
850 conditions (CCCP+, 60 min) (A) and quantification (B) of ATG9A colocalization with
851 mitochondria. Endogenous ATG9 was immunostained in penta KO cells expressing both

852 GFP–OPTN and mRuby–Ub or both GFP–OPTN Δ UBAN and anti-GFP nanobody–mRuby–
853 Ub (nano–mRuby–Ub) together with mitochondrially targeted Halo–SNAP (mtHalo–SNAP).
854 Scale bars indicate 4 μ m and 2 μ m (magnified images). Solid horizontal bars indicate the
855 means, each dot indicates the mean value from one field of view with \geq 10 cells (n=15).
856 Differences were statistically analyzed by Welch's two-tailed *t* test.
857 (C and D) Representative data (C) and quantification (D; p=0.99) of organelle
858 immunoprecipitation in cells expressing GFP–OPTN or GFP–OPTN Δ UBAN in the presence
859 or absence of FLAG-ATG9A. ATG9 vesicles were immunoprecipitated by FLAG M2 beads
860 and GFP was blotted to detect the interaction between GFP–OPTN (WT or Δ UBAN) and
861 ATG9 vesicles at 60 min after CCCP treatment. Solid horizontal bars indicate the means,
862 and dots indicate the data from five independent experiments. Differences were statistically
863 analyzed by Welch's two-tailed *t* test.
864 (E) The models of ATG9 vesicle recruitment (left) and isolation membrane elongation (right)
865 mediated by liquid-like OPTN condensates. Partial or complete wetting of phase-separated
866 OPTN enables the recruitment of ATG9 vesicles to ubiquitinated mitochondria (left). Wetting
867 of OPTN on mitochondria and isolation membranes also facilitates the engulfment of
868 mitochondria by the isolation membranes (right).

869

870 **Figure EV1. Localization of autophagy adaptors between mitochondria during**
871 **Parkin-mediated mitophagy.**

872 (A) Representative images (left) and spline graphs of the intensity profiles along the
873 indicated arrows (from position 0; right) of wild-type HeLa cells expressing one of the GFP–
874 tagged autophagy adaptors or ubiquitin and mRuby–Omp25 at 45 min after CCCP
875 treatment. Mitochondrial clusters (Mt–Mt) are shown. The y-axis in each of the graphs
876 indicates the fluorescence intensity.
877 (B) The relative intensity of each adaptor was calculated as in Figure 1C. Solid horizontal
878 bars indicate the means, and dots indicate the data from five structures. Differences were
879 statistically analyzed by one-way ANOVA with Dunnett's post-hoc test.

880 (C) Representative images (left) and spline graphs of the intensity profiles along the
881 indicated arrows (from position 0; right) of HeLa cells lacking all five autophagy adaptors
882 (penta KO cells) expressing one of the GFP-tagged autophagy adaptors or ubiquitin and
883 mRuby–Omp25 at 45 min after CCCP treatment. Mitochondrial clusters (Mt–Mt) are shown.

884 The y-axis in each of the graphs indicates the fluorescence intensity.

885 (D) The relative intensity of each adaptor was calculated as in Figure 1C. Solid horizontal
886 bars indicate the means, and dots indicate the data from five structures. Differences were
887 statistically analyzed by one-way ANOVA with Dunnett's post-hoc test.

888

889 **Figure EV2. p62 on mitochondrial clusters and OPTN and NDP52 at the**
890 **mitochondria-isolation membrane contact sites are resistant to 1,6-hexanediol**
891 **treatment.**

892 (A) Penta KO cells expressing GFP–p62 at 45 min after CCCP treatment. Images of cells
893 before (left) and 2 min after (right) the addition of 10% 1,6-hexanediol are displayed. Scale
894 bars, 5 μ m and 2 μ m (magnified images).

895 (B) Penta KO cells expressing GFP–OPTN (left) or GFP–NDP52 (right) at 45 min after
896 CCCP treatment. Images of cells before (upper panels) and 2 min after (lower panels) the
897 addition of 10% 2,5-hexanediol are displayed. Scale bars, 5 μ m and 2 μ m (magnified
898 images).

899 (C) Penta KO cells expressing GFP–OPTN (left) or GFP–NDP52 (right) at 45 min after
900 CCCP treatment. Mitochondria associated with isolation membranes (LC3) were analyzed.
901 Images of cells before (upper panels) and 2 min after (lower panels) the addition of 10%
902 1,6-hexanediol are displayed. Scale bars, 5 μ m and 2 μ m (magnified images).

903

904 **Figure EV3: Droplet distribution depends on the binding strength.**

905 (A) Dependence of droplet distribution on two mitochondria on Ub-binding strength (χ_{Ub})
906 and self-binding strength (χ_{self}). Mitochondrial area exclusion (χ_{Mt}) and surface tension (σ)
907 were set to $\chi_{Mt} = 5k_B T$ and $\sigma = k_B T$, respectively.

908 (B) Dependence of droplet distribution on isolation membrane and mitochondria on LC3-
909 binding strength (χ_{LC3}). The other parameters were set to $\chi_{Mt} = 5k_B T$, $\sigma = k_B T$, $\chi_{self} =$
910 $3k_B T$ and $\chi_{Ub} = 12k_B T$. The bending angle of the isolation membrane was set to $\alpha = \pi/3$.

911

912 **Figure EV4. Loss of mobility and mitophagy activity with ubiquitin binding mutants**
913 **of OPTN.**

914 (A) Penta KO cells expressing both GFP–OPTN and mRuby–Ub (i), GFP–OPTN (E478G)
915 and mRuby–Ub (ii), both GFP–OPTN (E478G) and anti-GFP nanobody–mRuby–Ub (iii),
916 both GFP–OPTNΔUBAN and anti-GFP nanobody–mRuby–Ub (iv), and both
917 OPTNΔUBAN–GFP and anti-GFP nanobody–mRuby–Ub (v) at 45 min after CCCP
918 treatment. Time-lapse images of GFP FRAP are shown. Photobleached areas are circled
919 by dotted lines. Scale bars indicate 4 μ m and 2 μ m (magnified images).

920 (B) Quantification of GFP FRAP on separate mitochondria (Mt) in penta KO cells
921 expressing both GFP–OPTN and mRuby–Ub (i), both GFP–OPTN (E478G) and anti-GFP
922 nanobody–mRuby–Ub (iii), both GFP–OPTNΔUBAN and anti-GFP nanobody–mRuby–Ub
923 (iv), and both OPTNΔUBAN–GFP and anti-GFP nanobody–mRuby–Ub (v) at 45 min after
924 CCCP treatment. Data were collected from four structures and were fitted to the equation y
925 $= a * (1 - \exp(-b * x))$. The dark shading represents the 95% confidence intervals, and the
926 light shading represents the 95% prediction intervals.

927 (C and D) Representative data (C) and quantification (D) of HaloTag (Halo) processing
928 assay using cells expressing the indicated OPTN and Ub constructs. Cells expressing the
929 mtHalo–SNAP mitophagy reporter were treated without (0 h) and with oligomycin and
930 antimycin for 18 h. The amount of processed Halo (proc. Halo) indicates the relative
931 amount of mitochondria degraded in lysosomes. Solid horizontal bars indicate the means,
932 and dots indicate the data from three independent cultures. Differences were statistically
933 analyzed by one-way analysis of variance with Dunnett's post-hoc test.

934

935 **Figure EV5. Recruitment of TBK1 and FIP200 during mitophagy.**

936 (A, B) Localization of FIP200 and phosphorylated TBK1 under mitophagy-inducing
937 conditions (CCCP, 60 min). Endogenous FIP200 (A) and phosphorylated TBK1 (B) were
938 immunostained in penta KO cells expressing both GFP–OPTN and mRuby–Ub or both
939 GFP–OPTN Δ UBAN and anti-GFP nanobody–mRuby–Ub together with mitochondrially
940 targeted Halo–SNAP (mtHalo–SNAP). Scale bars indicate 4 μ m and 2 μ m (magnified
941 images).

942

Figure 1

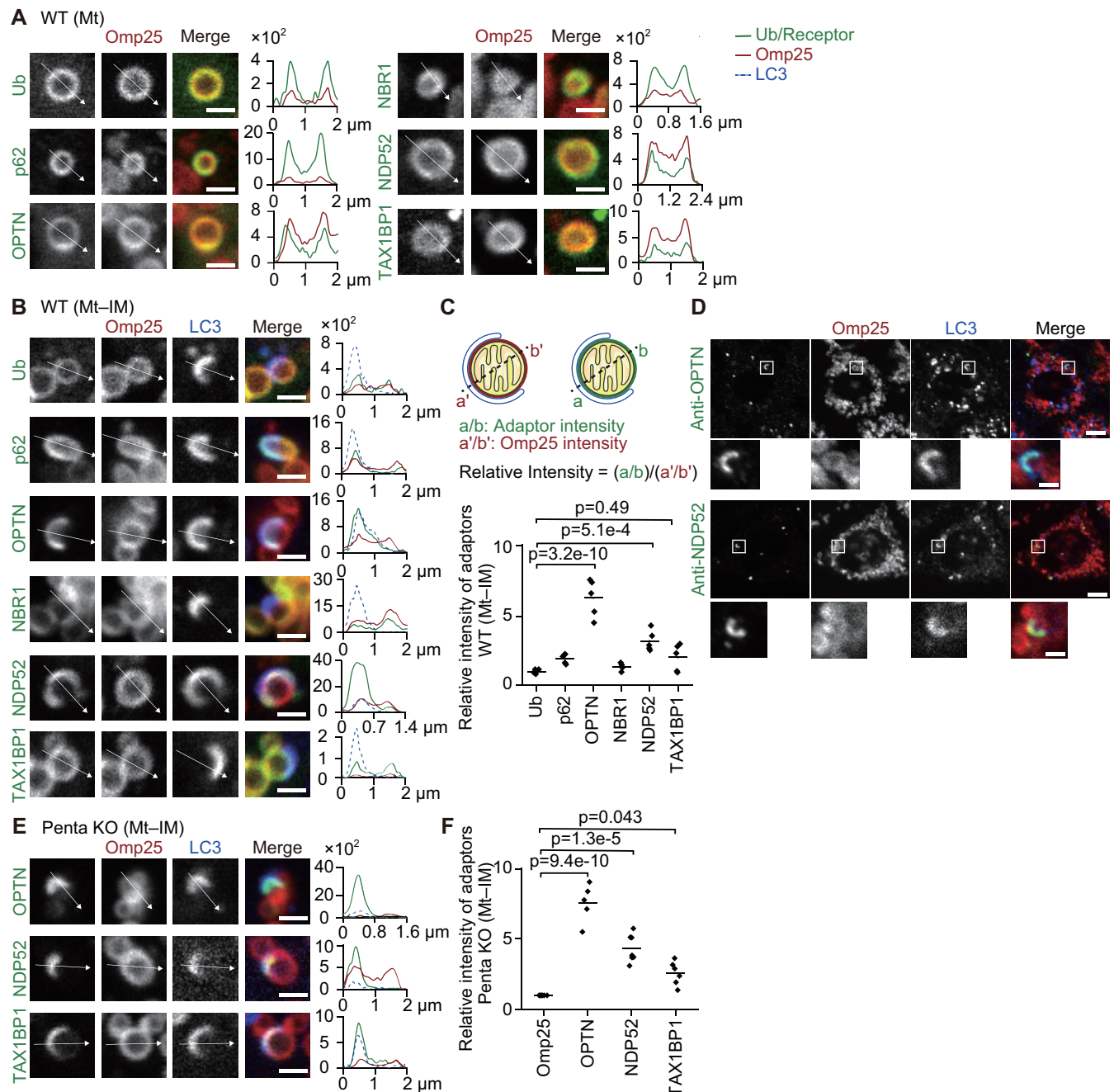


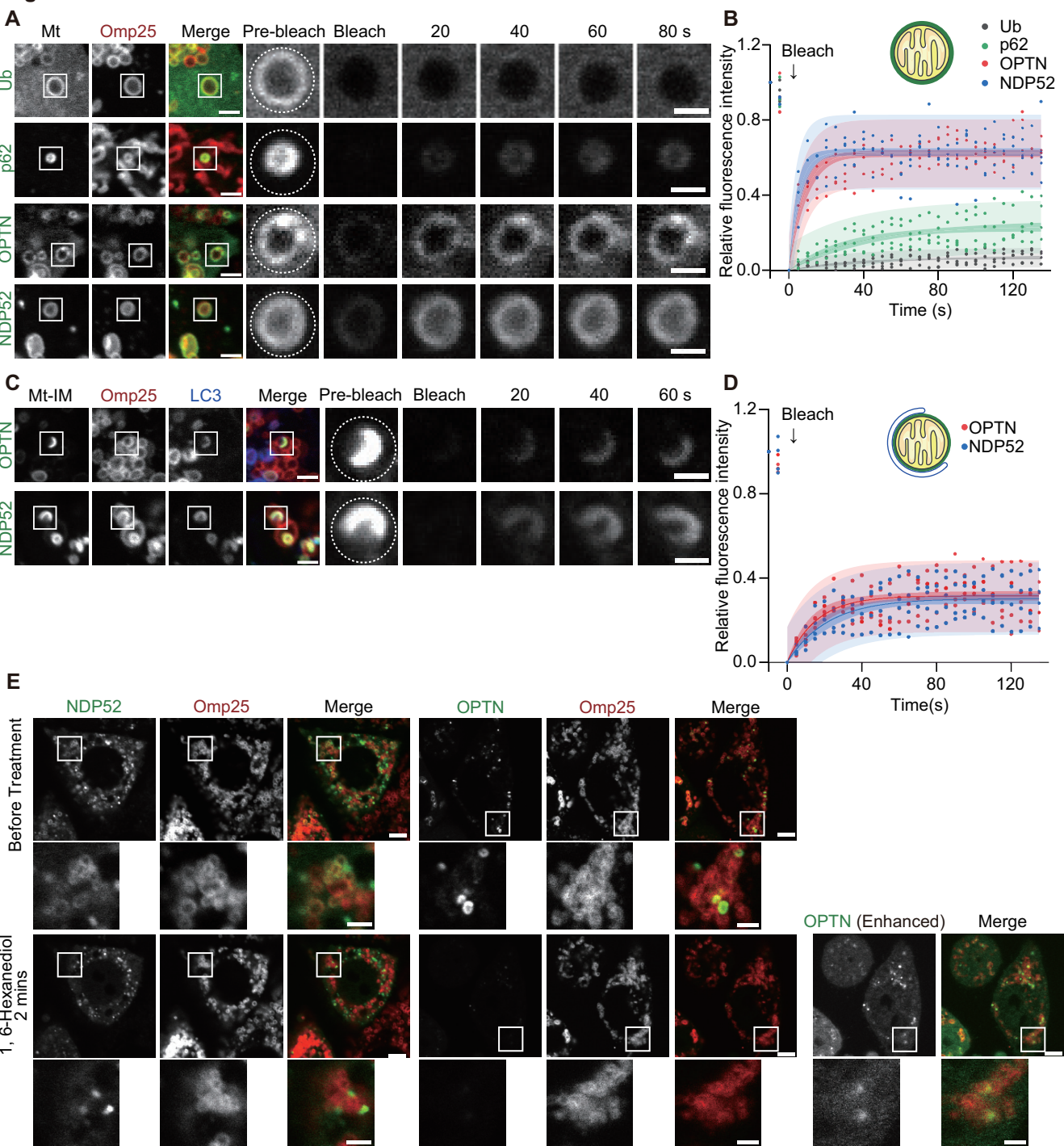
Figure 2

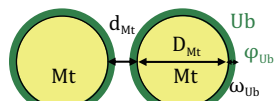
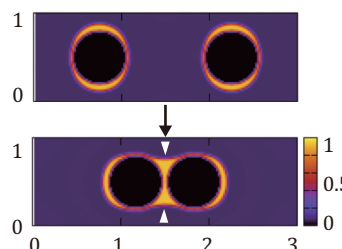
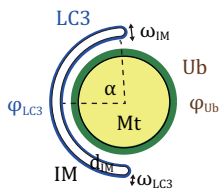
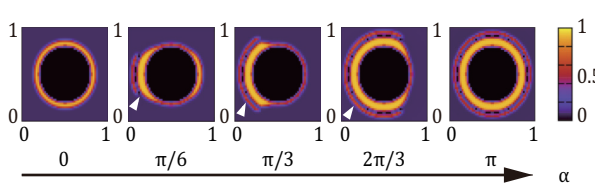
Figure 3**A****B****C****D**

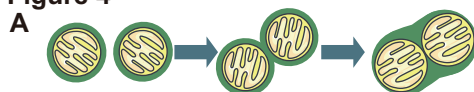
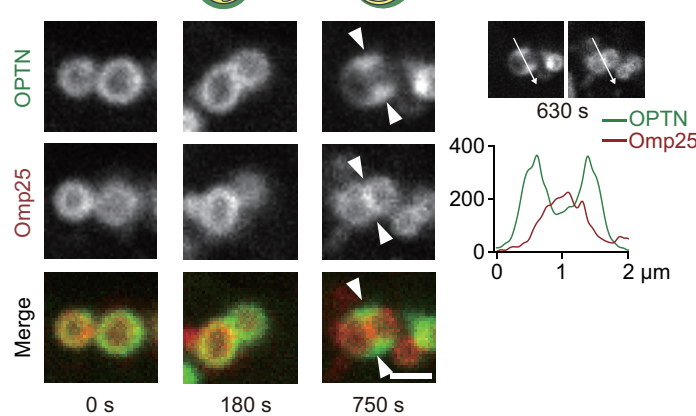
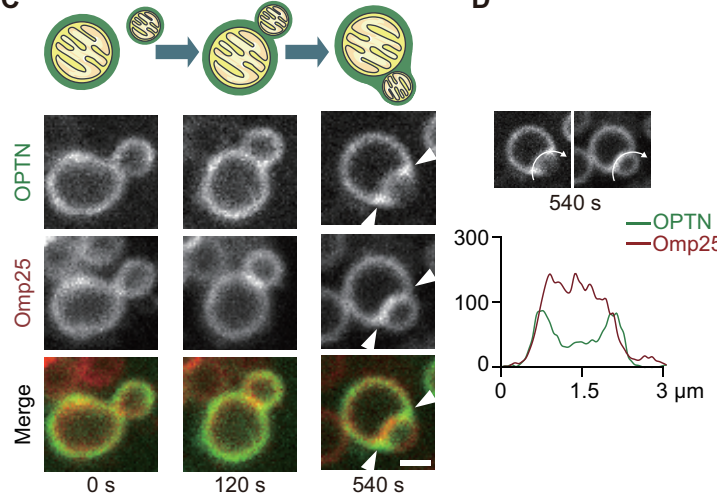
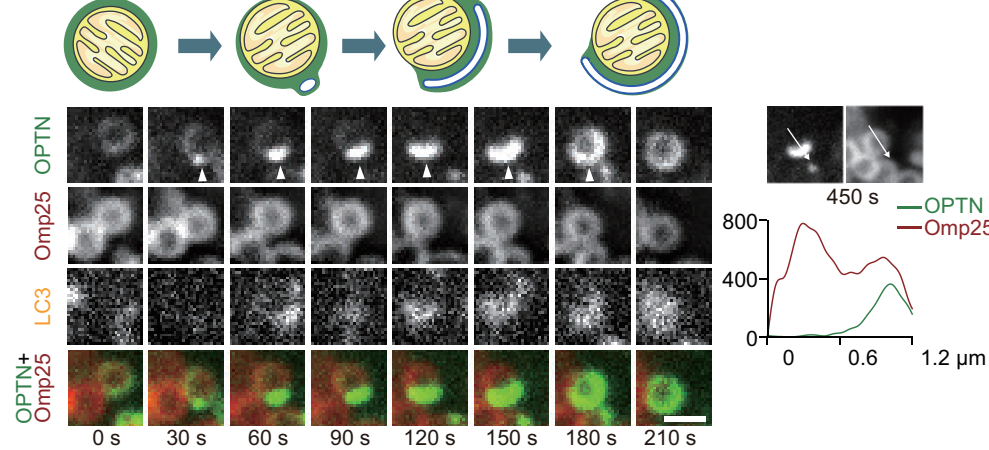
Figure 4**B****C****D****E****F**

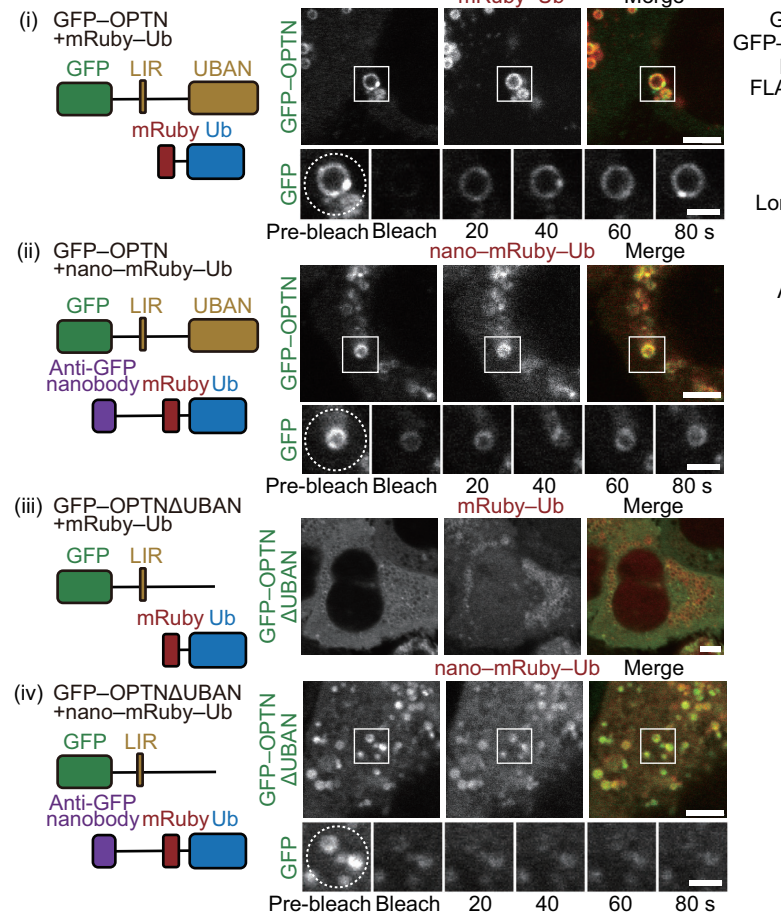
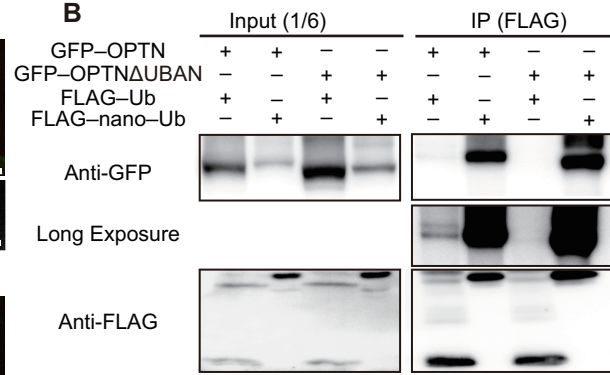
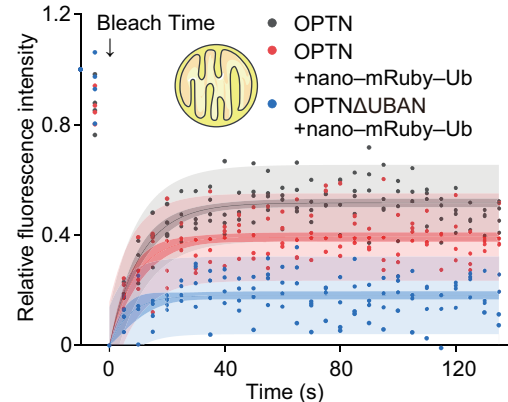
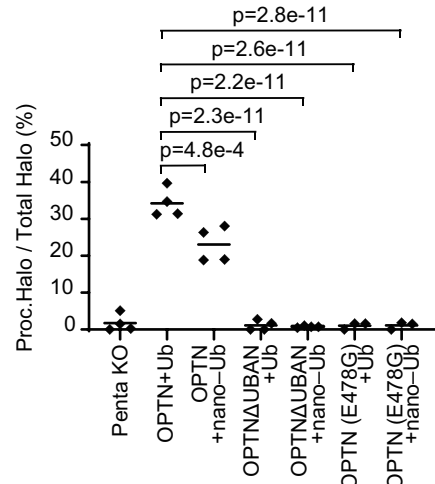
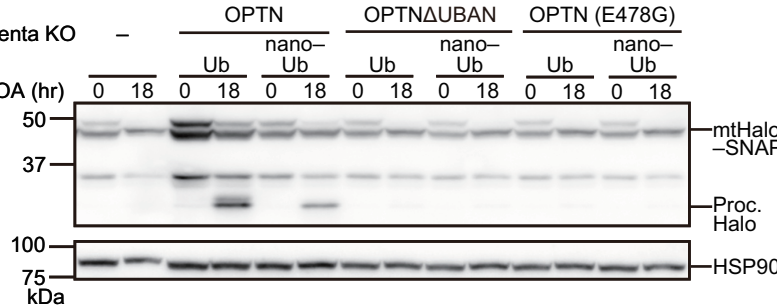
Figure 5**A****B****C****E****D**

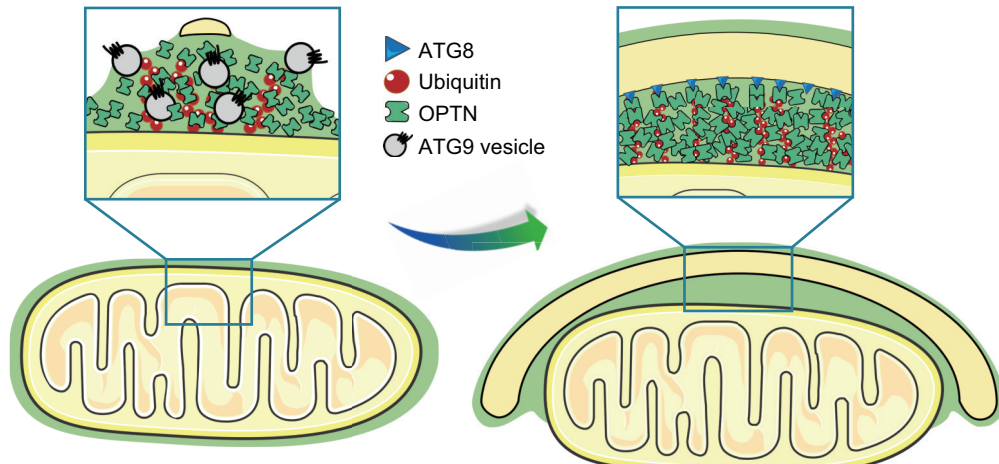
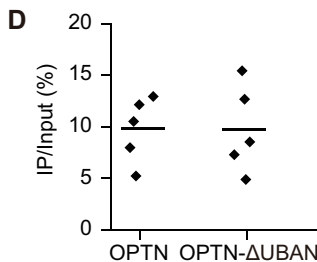
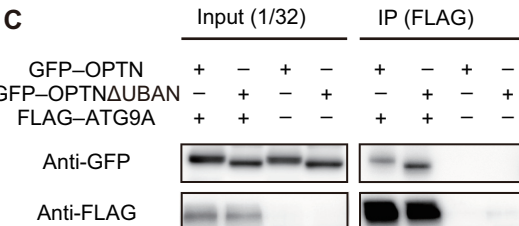
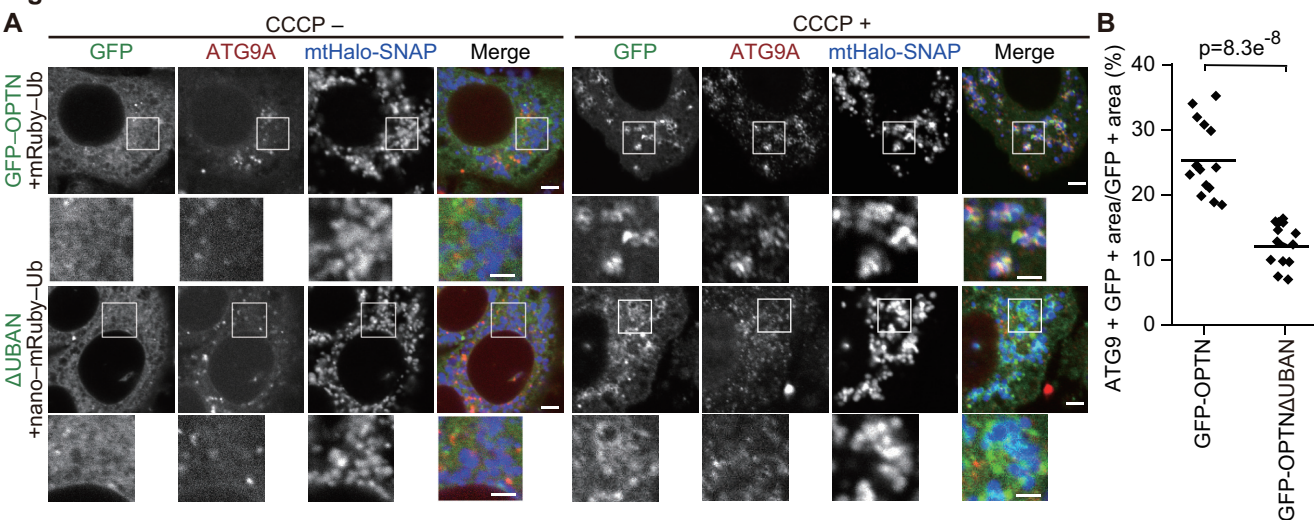
Figure 6

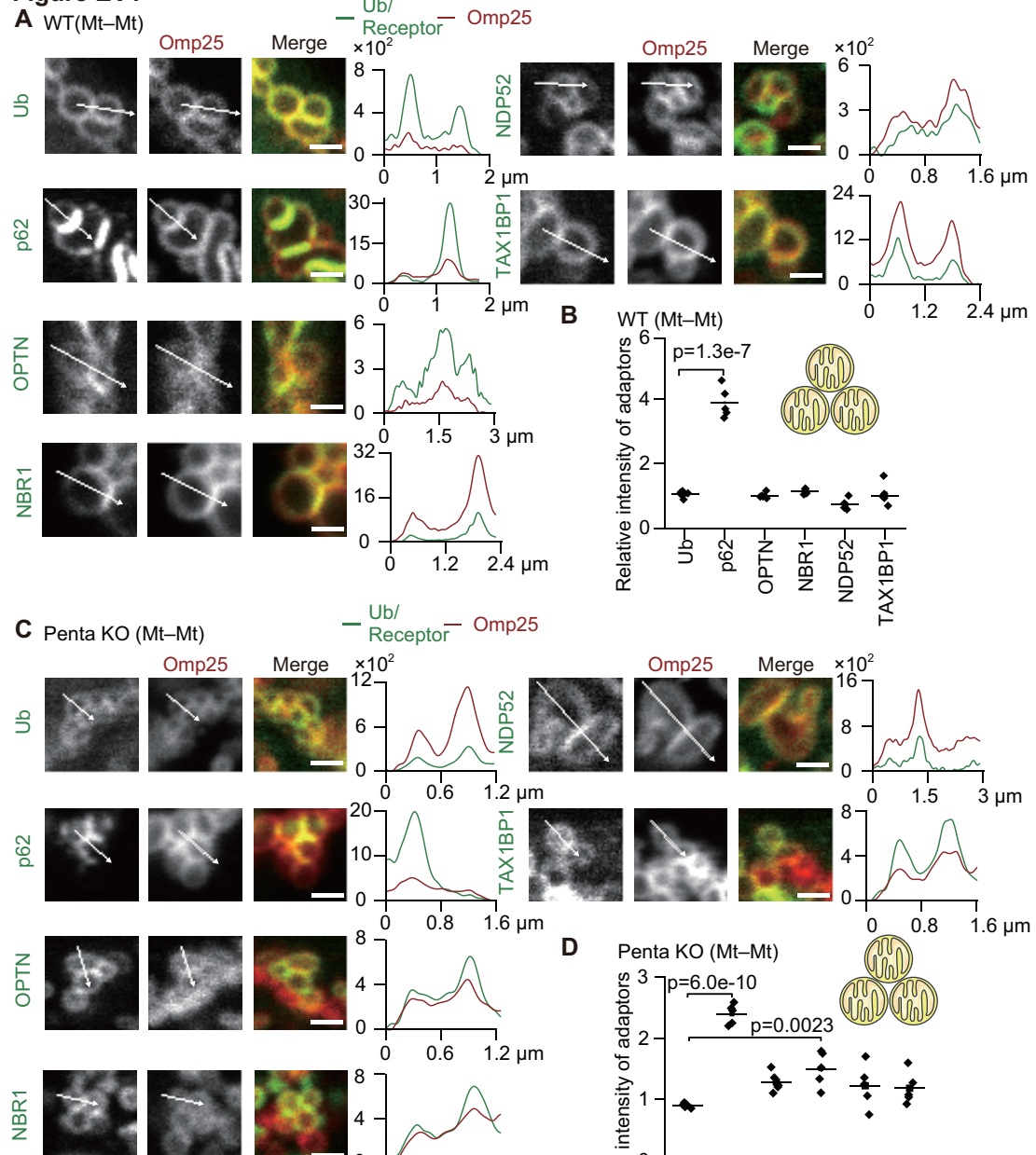
Figure EV1

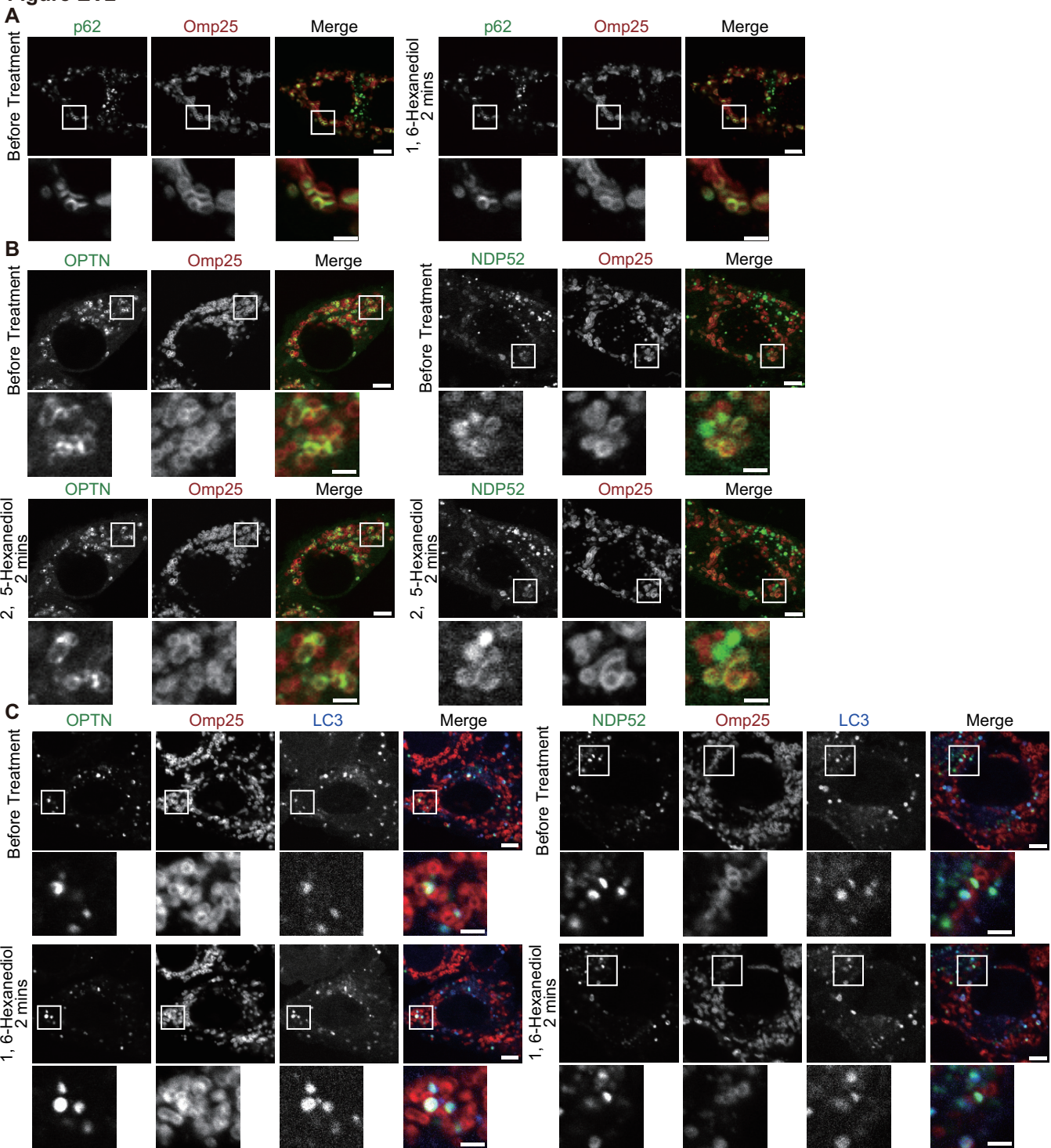
Figure EV2

Figure EV3

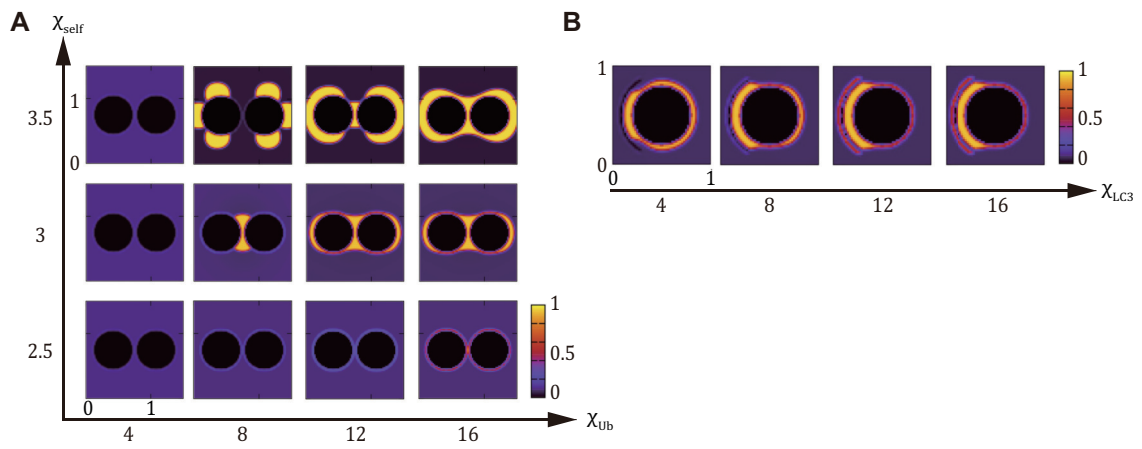


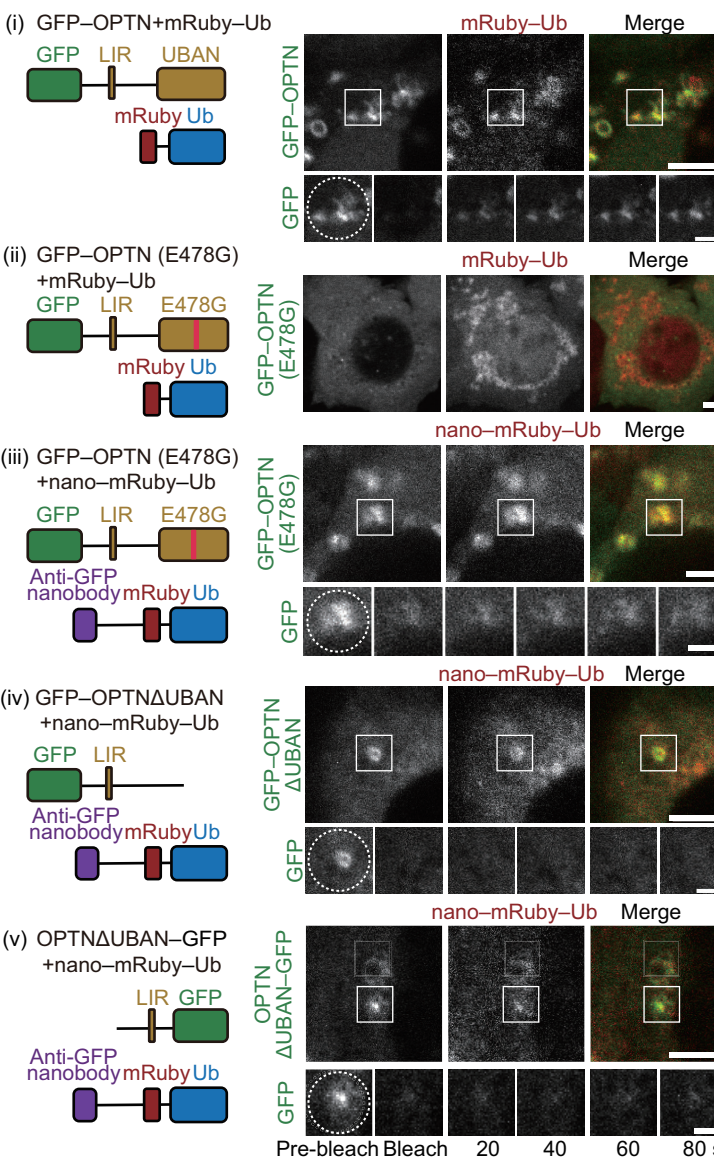
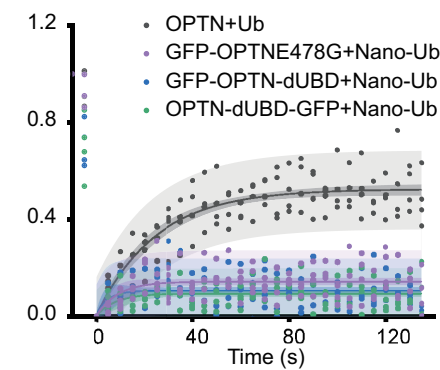
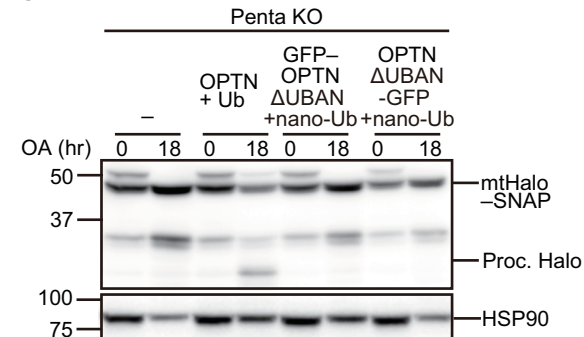
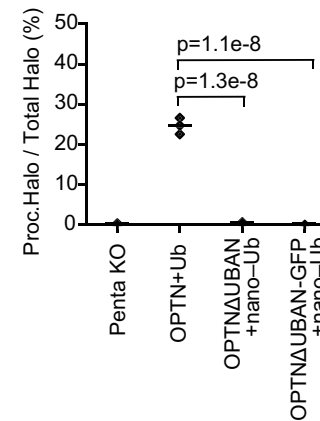
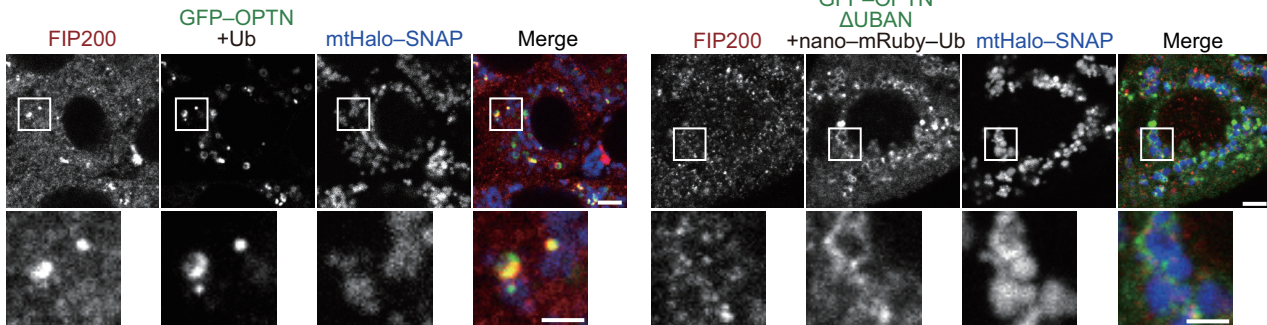
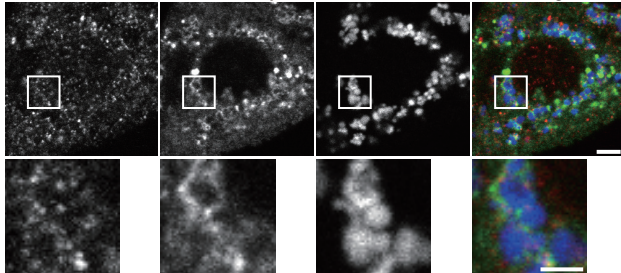
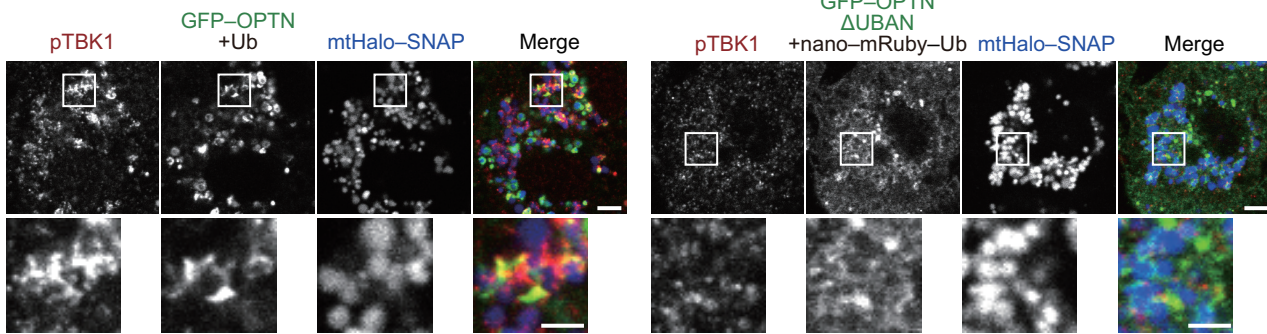
Figure EV4**A****B****C****D**

Figure EV5**A**GFP-OPTN
 Δ BAN

FIP200 +nano-mRuby-Ub mtHalo-SNAP Merge

**B**GFP-OPTN
 Δ BAN

pTBK1 +nano-mRuby-Ub mtHalo-SNAP Merge

